

# Origin of the Intraseasonal Variability over the North Pacific in Boreal Summer\*

LU WANG

*The National Key Laboratory of Numerical Modeling for Atmospheric Sciences and Geophysical Fluid Dynamics,  
Institute of Atmospheric Physics, Chinese Academy of Sciences, and National Satellite Meteorological  
Center, Beijing, China*

TIM LI

*International Pacific Research Center and Department of Meteorology, University of Hawaii at Manoa, Honolulu, Hawaii*

TIANJUN ZHOU

*The National Key Laboratory of Numerical Modeling for Atmospheric Sciences and Geophysical Fluid Dynamics,  
Institute of Atmospheric Physics, Chinese Academy of Sciences, Beijing, China*

XINYAO RONG

*Chinese Academy of Meteorological Sciences, Beijing, China*

(Manuscript received 30 November 2011, in final form 28 July 2012)

## ABSTRACT

The spatial structure and temporal evolution of the intraseasonal oscillation (ISO) in boreal summer over the midlatitude North Pacific Ocean are investigated, through the diagnosis of NCEP reanalysis data. It is found that the midlatitude ISO has an equivalent-barotropic structure, with maximum amplitude at 250 hPa. Initiated near 120°W, the ISO perturbation propagates westward at a phase speed of about 2.4 m s<sup>-1</sup> and reaches a maximum amplitude at 150°W. A diagnosis of barotropic energy conversion shows that the ISO gains energy from the summer mean flow in the ISO activity region. A center-followed column-averaged vorticity budget analysis shows that the nonlinear eddy meridional vorticity transport plays a major role in the growth of the ISO perturbation. There is a two-way interaction between ISO flows and synoptic eddies. While a cyclonic (anticyclonic) ISO flow causes synoptic-scale eddies to tilt toward the northwest–southeast (northeast–southwest) direction, the tilted synoptic eddies then exert a positive feedback to reinforce the ISO cyclonic (anticyclonic) flow through eddy vorticity transport. The reanalysis data and numerical simulations show that the midlatitude ISO is primarily driven by local processes and the tropical forcing accounts for about 20% of total intraseasonal variability in midlatitudes. However, 20% might be an underestimate given that the tropical intraseasonal forcing is not fully included in the current observational analysis and modeling experiment.

## 1. Introduction

Since Madden and Julian (1971, 1972) discovered the 30–60-day oscillation of equatorial zonal wind

perturbations, a number of studies have been devoted to understanding the dynamics of the tropical intraseasonal oscillation (ISO) or the Madden–Julian oscillation (MJO), including its seasonality (e.g., Wang and Rui 1990; Madden and Julian 1994), planetary zonal wavelength selection (Li and Zhou 2009), horizontal and vertical structure (Hendon and Salby 1994; Wang and Li 1994; Sperber 2003; Zhang 2005), and phase propagation (Lau and Peng 1987; Li and Wang 1994; Jiang et al. 2004; Maloney 2009; Hsu and Li 2012).

The dynamics of the midlatitude ISO, on the other hand, has received much less attention. By analyzing the First Global Atmospheric Research Program (GARP)

---

\* School of Ocean and Earth Science and Technology Contribution Number 8781 and International Pacific Research Center Contribution Number 928.

---

*Corresponding author address:* Tim Li, IPRC and Department of Meteorology, University of Hawaii at Manoa, 2525 Correa Rd., Honolulu, HI 96822.  
E-mail: timli@hawaii.edu

Global Experiment (FGGE) data, Krishnamurti and Gadgil (1985) showed that strong signals with a period of about 45 days appeared in the midlatitude upper-level westerly jet exit. Different from the baroclinic vertical structure of the MJO, the midlatitude ISO exhibits a quasi-barotropic structure. The statistically significant midlatitude ISO signal (Ghil and Mo 1991; Kawamura et al. 1996) influences rainfall variability over both North America (Jiang and Lau 2008) and the Yangtze River valley of eastern China (Yang et al. 2010).

What is the origin of the midlatitude ISO? It has been hypothesized that the origin of the midlatitude ISO arises from a tropical forcing (Lau and Phillips 1986; Chen and Yen 1991; Kawamura et al. 1996; Pan and Li 2008). Lau and Phillips (1986) calculated correlations between 20–70-day outgoing longwave radiation (OLR) anomalies in the tropics and geopotential height anomalies at 500 hPa over the Northern Hemisphere in boreal winter and found two midlatitude wave trains, a Europe–western Pacific Ocean wave train and a central Pacific–North America wave train. Both of the wave trains are highly correlated with tropical convection anomalies. Chen and Yen (1991) suggested that the tropical convection could affect the midlatitude ISO through inducing divergent flows. Kawamura et al. (1996) showed that the MJO convection near the Philippine Sea could influence the midlatitude ISO through barotropic Rossby wave dispersion along the great circle route over the North Pacific.

There are also some studies suggesting that the midlatitude ISO is independent of tropical forcing (e.g., Knutson and Weickmann 1987; Ghil and Mo 1991). Liebmann and Hartmann (1984) found that the MJO forcing accounted for a small fraction of the total midlatitude ISO variance. Wang et al. (2012) suggested that the local air–sea interaction may play a role in the phase transition of atmospheric intraseasonal oscillations over the Kuroshio Extension region. Their analysis revealed that intraseasonal SST variability over the midlatitude northern Pacific was caused by local atmospheric forcing through the change of intraseasonal shortwave radiation and latent heat flux anomalies. The SST anomalies, on the other hand, could help the transition of the atmospheric ISO through changing the atmospheric convective instability and inducing convective heating.

The objective of the present study is to reveal the origin of the midlatitude ISO through reanalysis data and numerical model experiments. We investigate the specific dynamic processes that give rise to the initiation, growth, and propagation of the midlatitude ISO and compare the relative roles of tropical versus midlatitude processes. Because the activity centers of the midlatitude ISO differ significantly between summer and winter, we focus on a general boreal summer (May–October) season in this study.

The remainder of the paper is organized as follows. After describing the data, methods, and model design used in this study in section 2, we show the structural and evolutionary characteristics of the ISO over the midlatitude North Pacific in section 3. Then, the energy source, dynamic mechanism, and initiation of the midlatitude ISO are studied in section 4. The relative contributions of the local atmospheric dynamics and the tropical forcing are examined in section 5. A summary is given in section 6.

## 2. Data, methods, and numerical experiments

### a. Data

This study primarily uses the U.S. National Centers for Environmental Prediction–Department of Energy (NCEP–DOE) reanalysis data from 1979 to 2009 (Kanamitsu et al. 2002). Daily averaged zonal  $u$  and meridional winds  $v$ , pressure vertical velocity  $\omega$ , geopotential  $\phi$ , temperature  $T$ , and pressure  $p$  from 1000 to 100 hPa are utilized. Then, the relative vorticity  $\zeta$  and streamfunction  $\psi$  calculated with  $u, v$  are also used. The horizontal resolutions of these dynamic and thermodynamic variables are  $2.5^\circ$  longitude  $\times$   $2.5^\circ$  latitude.

### b. Filtering and vorticity budget analysis

In this study, the Lanczos bandpass filter (Duchon 1979) was used to extract the intraseasonal fields. The climatologic annual cycle was removed prior to the filtering. As will be shown by the power spectrum analysis of the midlatitude geopotential height in section 3, the spectrum peak of intraseasonal signal is in the band of 10–50 days. So in this study, the ISO field is defined with periods of 10–50 days and denoted by a prime.

To examine factors that contribute to the growth of a moving anomalous intraseasonal system, a vorticity budget analysis on a Lagrangian frame was adopted. As the midlatitude ISO has an equivalent-barotropic vertical structure, we diagnose a column-averaged vorticity budget. Because the ISO perturbation primarily propagates zonally, the rate of change of the relative vorticity following the motion can be written as

$$\frac{D[\zeta']}{Dt} = \frac{\partial[\zeta']}{\partial t} + C_x \frac{\partial[\zeta']}{\partial x}, \quad (1)$$

where

$$\begin{aligned} \frac{\partial[\zeta']}{\partial t} = & \{[-\mathbf{V} \cdot \nabla(\zeta + f)]'\} - \left[ \left( \omega \frac{\partial \zeta}{\partial p} \right)' \right] \\ & - \{[(\zeta + f)\nabla \cdot \mathbf{V}]'\} + \left[ \left\{ \mathbf{k} \cdot \left( \frac{\partial \mathbf{V}}{\partial p} \times \mathbf{v}\omega \right) \right\}' \right], \quad (2) \end{aligned}$$

square brackets denote the vertical average between  $p_o = 1000$  hPa and  $p_s = 100$  hPa, that is,

$$\frac{1}{p_o - p_s} \int_{p_o}^{p_s} A dp,$$

and  $C_x$  is the zonal phase speed of the system,  $t$  denotes time, and  $f$  is the Coriolis parameter. The first term on the right-hand side of Eq. (1) represents the rate of change of the local intraseasonal vorticity anomaly, which is given by the sum of four terms [see Eq. (2)]: the horizontal advection of absolute vorticity, the vertical advection of relative vorticity, the divergence term, and the twisting term (Holton 2004).

A variable may be separated into three components, the low-frequency background state (LFBS; >50 days) and intraseasonal (10–50 days) and synoptic-scale (3–10 days) parts:

$$A = \bar{A} + A' + A'', \tag{3}$$

where a single overbar denotes the LFBS field and a double prime denotes the synoptic-scale field.

As a result of the above decomposition, the intraseasonal meridional vorticity advection anomaly can be expressed as

$$\begin{aligned} -\left(v \frac{\partial \zeta}{\partial y}\right)' &= -\left\{(\bar{v} + v' + v'') \frac{\partial(\bar{\zeta} + \zeta' + \zeta'')}{\partial y}\right\}' = -\left(\bar{v} \frac{\partial \zeta'}{\partial y}\right)' - \left(v' \frac{\partial \bar{\zeta}}{\partial y}\right)' - \left(v' \frac{\partial \zeta'}{\partial y}\right)' - \left(v' \frac{\partial \zeta''}{\partial y}\right)' - \left(v'' \frac{\partial \zeta'}{\partial y}\right)' \\ &\quad - \left(v'' \frac{\partial \zeta''}{\partial y}\right)' - \left(v'' \frac{\partial \bar{\zeta}}{\partial y}\right)' - \left(\bar{v} \frac{\partial \zeta''}{\partial y}\right)' - \left(\bar{v} \frac{\partial \zeta''}{\partial y}\right)'. \end{aligned} \tag{4}$$

*c. Barotropic energy conversion and wave activity*

The barotropic energy conversion between the summer mean flow and the ISO flow, and the barotropic energy conversion between the summer mean flow and the synoptic motion, are both examined. Following Hoskins et al. (1983), the energy conversion terms may be written as

$$\overline{\overline{\text{CK}}}_{\text{iso}} = \frac{\overline{v'^2 - u'^2}}{2} \left(\frac{\partial \bar{u}}{\partial x} - \frac{\partial \bar{v}}{\partial y}\right) - \overline{u'v'} \left(\frac{\partial \bar{u}}{\partial y} + \frac{\partial \bar{v}}{\partial x}\right) \quad \text{and} \tag{5}$$

$$\overline{\overline{\text{CK}}}_{\text{ssv}} = \frac{\overline{v''^2 - u''^2}}{2} \left(\frac{\partial \bar{u}}{\partial x} - \frac{\partial \bar{v}}{\partial y}\right) - \overline{u''v''} \left(\frac{\partial \bar{u}}{\partial y} + \frac{\partial \bar{v}}{\partial x}\right), \tag{6}$$

where a double overbar denotes the summer mean state. A positive value of  $\overline{\overline{\text{CK}}}_{\text{iso}}$  represents energy conversion from the mean flow to the ISO flow, and a positive value of  $\overline{\overline{\text{CK}}}_{\text{ssv}}$  represents energy conversion from the mean flow to the synoptic motion.

To understand the energy accumulation of the ISO flow, a 2D wave-activity flux is evaluated according to Takaya and Nakamura (2001):

$$\overline{\overline{\mathbf{W}}} = \frac{1}{2|\bar{\mathbf{u}}|} \left\{ \begin{aligned} &\overline{\overline{\bar{u}(\psi_x'^2 - \psi' \psi_{xx}') + \bar{v}(\psi_x' \psi_y' - \psi' \psi_{xy}')}} \\ &\overline{\overline{\bar{u}(\psi_x' \psi_y' - \psi' \psi_{xy}') + \bar{v}(\psi_y'^2 - \psi' \psi_{yy}')}} \end{aligned} \right\}. \tag{7}$$

Here,  $\psi$  denotes the streamfunction and  $\mathbf{u} = (u, v)$  denotes the horizontal wind velocity. The wave activity flux is independent of wave phase and parallel to the

local group velocity of stationary Rossby waves (Tam and Li 2006).

*d. Numerical experiments*

To identify the relative contributions of the remote and local forcing, we design a set of sensitivity numerical experiments to separate the effect of the tropical ISO forcing from local processes. The atmospheric general circulation model (AGCM) used in the study is ECHAM4.6 developed by the Max Planck Institute for Meteorology (MPI; Roeckner et al. 1996). The model has a horizontal resolution of T42, with 19 vertical levels extending from the surface to 10 hPa. This AGCM was previously used to study the northward propagation of the ISO (Jiang et al. 2004) and for real-case MJO prediction (Fu and Wang 2009).

The first experiment is termed the Control run, in which the model is forced by the climatologic monthly-mean SST, derived from the Hadley Centre Global Sea Ice and Sea Surface Temperature (HadISST) data for 20 years (Rayner et al. 2003). The second experiment is termed the No\_Trop run, in which the model is forced by the same SST fields for 20 years as the Control run but a strong Newtonian-type damping [(2 days)<sup>-1</sup>] is applied to force the model's prognostic variables (such as  $u$ ,  $v$ , and  $T$ ) in the tropics (30°S–30°N) toward the model's climatologic annual cycle, which is retrieved by averaging the outputs from the 20-yr Control run. In the second experiment, the model domain is separated into three regions: a strong-damping region, a transition region, and a no-damping region. As the horizontal resolution of the model is T42, the strong-damping region

actually covers  $26.510^{\circ}\text{N}$ – $26.510^{\circ}\text{S}$ , where the damping coefficient is  $(2 \text{ days})^{-1}$ ; the transition region covers two rows of grids next to the strong-damping region (i.e.,  $29.301^{\circ}\text{N/S}$  and  $32.091^{\circ}\text{N/S}$ ), where the damping coefficient is linearly decreased (i.e.,  $2/3$  and  $1/3$  of the strong damping rate, respectively); and the no-damping region covers the remaining model grids, where the damping coefficient is zero. By doing so, the tropical intraseasonal variability is greatly suppressed, and its impact on higher-latitude regions is minimized. Thus, the difference between the intraseasonal variability derived from the Control run and the No\_Trop run can reflect how strong the effect of the tropical MJO forcing is on the midlatitude ISO.

To examine the sensitivity of the results to the damping rate and the latitudinal extent of the damping, respectively, another two experiments are conducted. The first additional sensitivity experiment is named the Damp\_Sensitivity run, in which the damping coefficient in the strong-damping region is reduced to  $(8 \text{ days})^{-1}$  and the other configurations are the same as the No\_Trop run. The second additional sensitivity experiment is named the Lat\_Sensitivity run, in which the strong-damping region covers  $15.348^{\circ}\text{N}$ – $15.348^{\circ}\text{S}$  and the transition region covers  $18.138^{\circ}\text{N/S}$  and  $20.929^{\circ}\text{N/S}$ , with the other configurations being the same as the No\_Trop run.

### 3. Structure and evolution characteristics of ISO in the North Pacific

A calculation of the standard deviation  $\sigma$  of 10–90-day filtered geopotential height and streamfunction fields shows that the maximum ISO activity center in the boreal summer is located over the region of  $45^{\circ}$ – $55^{\circ}\text{N}$ ,  $160^{\circ}$ – $140^{\circ}\text{W}$  in the upper troposphere (black rectangle marked in Fig. 1). The same activity center appears in the middle and lower troposphere, but with a considerably reduced amplitude. Prior to calculating the standard deviation, the climatologic annual cycle was removed.

To reveal the dominant periodicity, a power spectral analysis of the 250-hPa geopotential height over the activity center was performed (see Fig. 2). As expected, synoptic-scale (less than 10 days) variability in mid-latitudes is quite strong. In addition, there are significant peaks on the intraseasonal time scales, especially in the band of 10–50 days. The same spectrum peak is found in the 250-hPa streamfunction field (not shown). Thus, in the following analysis we use 10–50-day-bandpass filtered data to represent the midlatitude ISO.

An EOF analysis was performed on the intraseasonal streamfunction field  $\psi'$  at 250 hPa in the domain of  $40^{\circ}$ – $60^{\circ}\text{N}$ ,  $120^{\circ}\text{E}$ – $120^{\circ}\text{W}$  during 1979–2009 to extract the

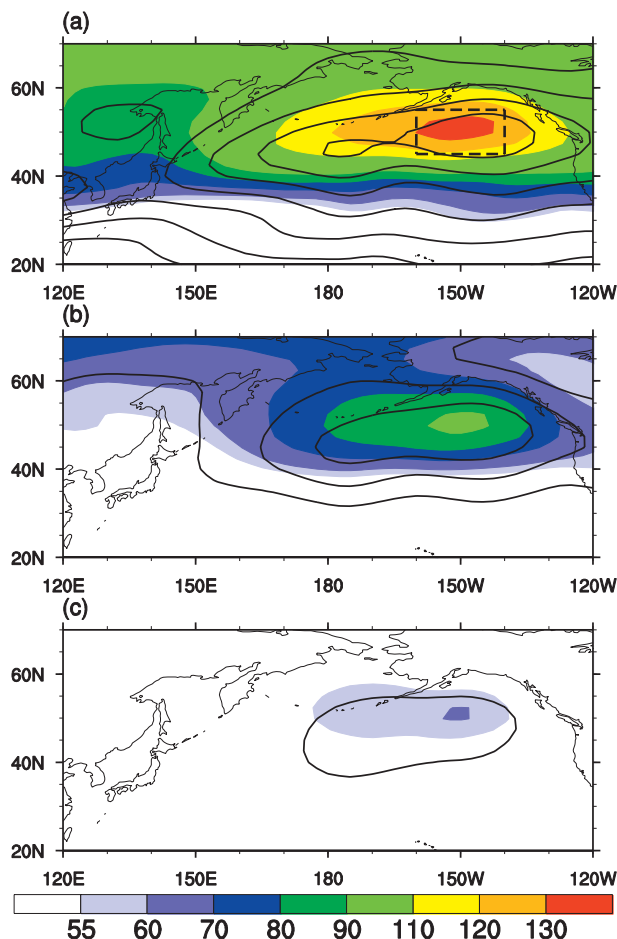


FIG. 1. (a) Standard deviation of 10–90-day filtered geopotential height anomalies (shaded;  $\text{m}$ ) and streamfunction anomalies (contour;  $\text{m}^2 \text{ s}^{-1}$ , with an interval of  $10^6 \text{ m}^2 \text{ s}^{-1}$ ) at 250 hPa during the boreal summer [May–October (MJJASO)]. (b) As in (a), but for 500 hPa. (c) As in (a), but for 850 hPa. The box in (a) marks the boreal summer ISO activity center. Note the irregular contour intervals in the color bar.

dominant ISO patterns (see Figs. 3a,b). The first mode, which explains 19.6% of the total variance, exhibits a large-scale cyclonic flow pattern centered at  $50^{\circ}\text{N}$ ,  $150^{\circ}\text{W}$ . The second mode, which explains 18.4% of the total variance, displays a zonal-oriented dipole with a cyclonic center at  $50^{\circ}\text{N}$ ,  $175^{\circ}\text{W}$  and an anticyclonic center at  $50^{\circ}\text{N}$ ,  $140^{\circ}\text{W}$ . According to North et al. (1982), the first two modes are not separable from each other but are statistically distinguished from the third mode in terms of the sampling error bars (see Table 1). Similar results were obtained when the EOF domain was expanded to  $90^{\circ}\text{W}$ , except that the combined first two EOF variance in a bigger domain is a little less (not shown).

The lead-lag correlation coefficients between principal component 1 (PC1) and PC2 (Fig. 3c) show that a maximum positive (negative) correlation occurs when

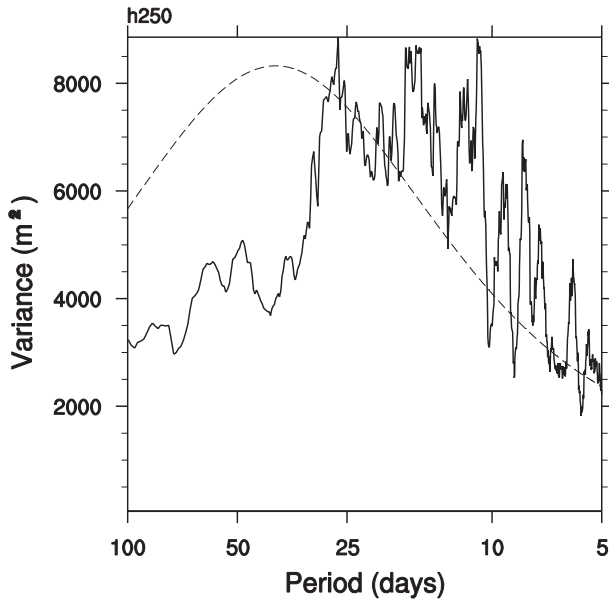


FIG. 2. Power spectral analysis of unfiltered geopotential height anomalies (with the annual cycle removed) averaged in the box marked in Fig. 1a at 250 hPa during boreal summer. The dashed line represents a 95% significance level. Note the irregularly distributed days in the x axis.

PC1 leads (lags) PC2 by 5 days and the maximum correlations exceed a 95% confidence level. It implies that the two leading modes represent the same physical mode with pronounced westward propagation over the midlatitude North Pacific.

The evolution pattern of  $\psi'$  at 250 hPa from day -10 to day 8, at an interval of 2 days, is shown in Fig. 4. This composite pattern is obtained by averaging the difference between the strong positive and negative ISO events. The strong positive events are defined when PC1's peak is above  $1.5\sigma$ , and the strong negative events are defined when PC1's minimum is below  $-1.5\sigma$ . Day 0 represents the time when the maximum/minimum vorticity (or minimum/maximum  $\psi'$ ) is located at  $50^\circ\text{N}$ ,  $150^\circ\text{W}$ . During the 31-yr period, 142 cases with 67 positive cases and 75 negative cases were selected for the composite analysis. At day -10, a large-scale anticyclonic anomaly is located at  $50^\circ\text{N}$ ,  $160^\circ\text{W}$ . Then it moves westward and reaches the longitude of  $180^\circ$  at day -6. Meanwhile, an anomalous cyclonic cell develops to the east of the anticyclone and propagates westward. The anomalous cyclonic circulation amplifies and attains its peak at day 0, and then it decays while continuing to move westward. The average westward speed of the intraseasonal cyclonic anomalies is about  $2.4 \text{ m s}^{-1}$ . Although the composite maps are derived from the time series of PC1, the circulation pattern at day 6 resembles the second EOF mode, which provides additional support

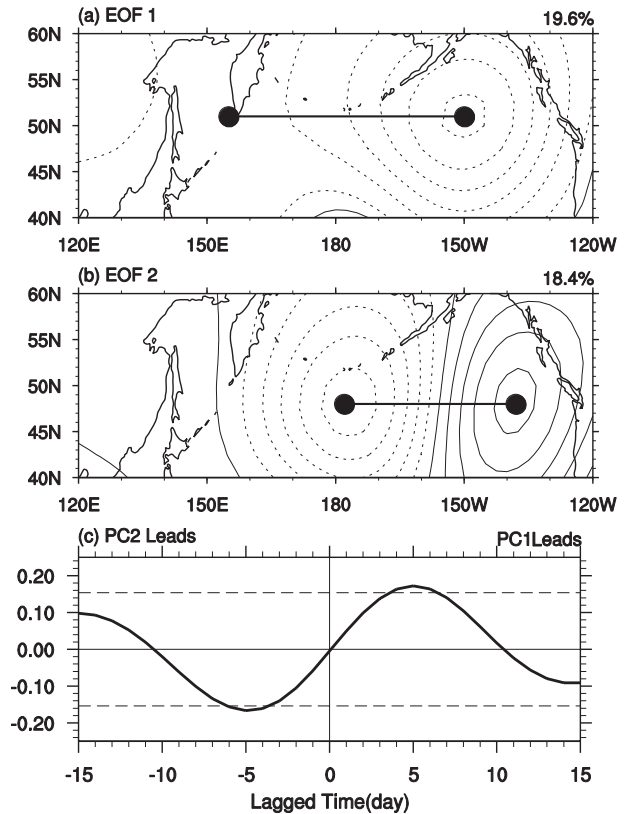


FIG. 3. (a) The pattern of the first EOF mode of the 10–50-day filtered streamfunction anomalies  $\psi'$  at 250 hPa during the boreal summer (solid line: positive; dashed line: negative). The corresponding variance is marked in the upper-right corner. The distance between two dot points indicates the half zonal wavelength of  $\psi'$ . (b) As in (a), but for the second EOF mode. (c) The lead-lag correlation coefficients between PC1 and PC2. The dashed line represents a 95% significance level.

that the two leading EOF modes represent different phases of the same physical mode.

To examine the vertical structure of the midlatitude ISO mode, Fig. 5 displays the longitudinal-vertical sections of anomalous geopotential height  $H'$  and temperature  $T'$  fields. At day -10, a warm (cold) center appears below (above) a positive height center near  $160^\circ\text{W}$ . The positive  $T'$  and  $H'$  gradually decay as they move westward from day -10 to day -6. Meanwhile, a negative height anomaly (coupled with a reversed cold-warm couplet) develops to its east. The low pressure system

TABLE 1. Fractional variance (%) explained by the first four EOF modes and the associated unit standard deviation of the sampling errors. The efficient sample sizes are estimated based on Chen (1982).

EOF1	EOF2	EOF3	EOF4
$19.6 \pm 1.08$	$18.4 \pm 1.02$	$14 \pm 0.77$	$10 \pm 0.55$

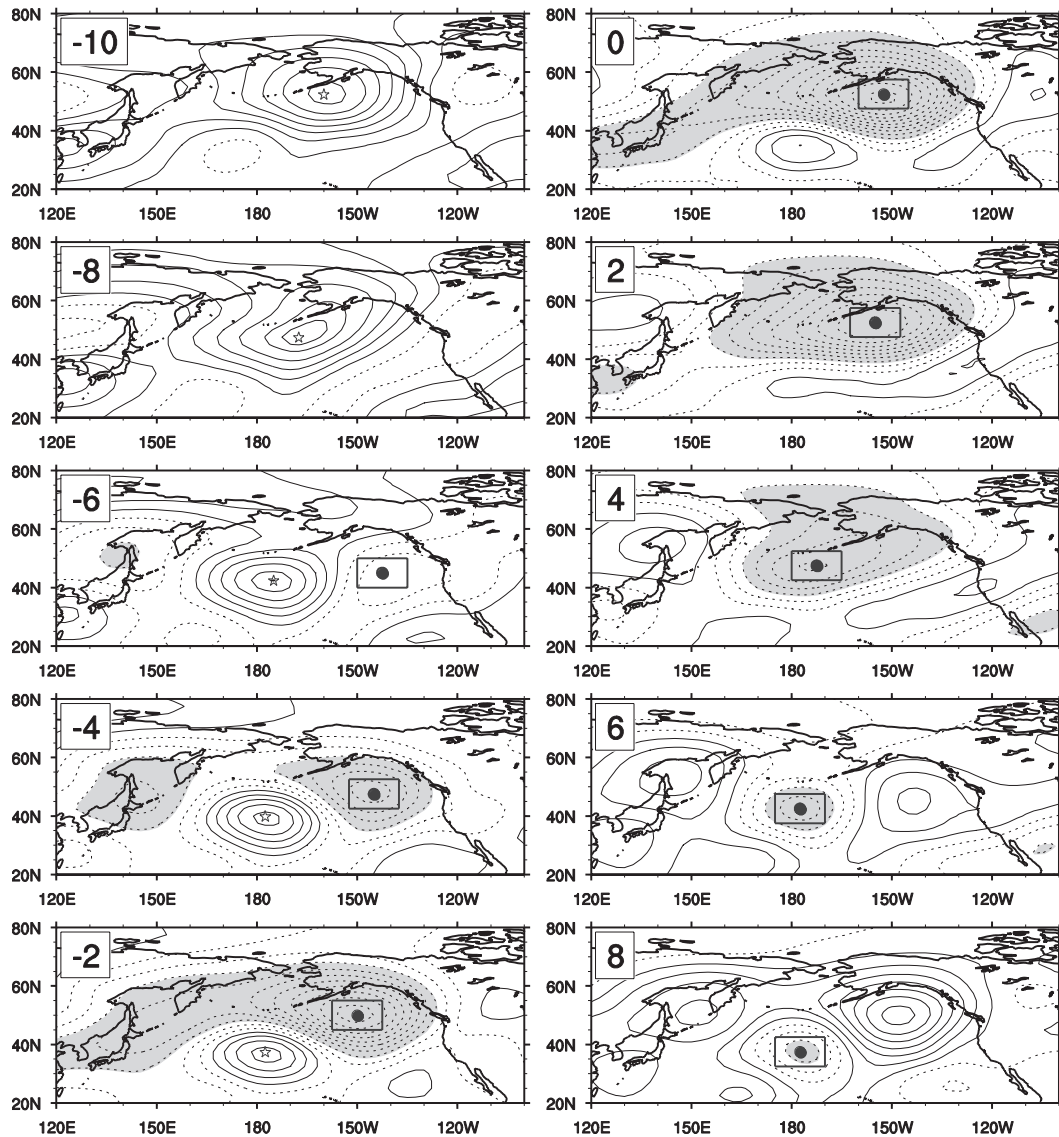


FIG. 4. Evolution of the composite 10–50-day filtered streamfunction anomalies  $\psi'$  (contour; solid line indicates positive values and the dotted line indicates negative ones;  $\text{m}^2 \text{s}^{-1}$ ) at 250 hPa from day  $-10$  to day 8, with an interval of 2 days. Values less than  $-3 \times 10^6 \text{ m}^2 \text{ s}^{-1}$  are shaded. Day 0 is a reference time corresponding to the peaks in the time series of the first EOF mode for each selected strong ISO case. The dots (stars) indicate the negative (positive) centers of  $\psi'$ .

has an equivalent-barotropic structure, with a maximum center located at 250 hPa. It intensifies as it propagates westward from day  $-6$  to day 0 and reaches a peak at day 0. The evolution of  $T'$  and  $H'$  after day 0 displays a mirror image as the days before. The averaged westward phase speed from day  $-6$  to day 6 is the same as that of  $\psi'$ .

#### 4. Energy source and growth mechanism of the ISO in the North Pacific

In this section, we address the following questions. Why does the maximum intraseasonal perturbation exist

in the region of the westerly jet exit (see Fig. 1)? Why does the ISO favor westward propagation while in the same region the synoptic perturbations move eastward? What is the mechanism for the growth of the ISO perturbation as it propagates westward? What initiates the ISO perturbation in the far eastern North Pacific?

##### a. Barotropic energy conversion

Figure 7a, described below, shows the horizontal distribution of the ISO-related  $\overline{\text{CK}}$  ( $\overline{\text{CK}}_{\text{ISO}}$ ) at 250 hPa. The maximum positive center of  $\overline{\text{CK}}_{\text{ISO}}$  is located in the eastern North Pacific near  $150^\circ\text{W}$  (see the box in Fig. 6a),

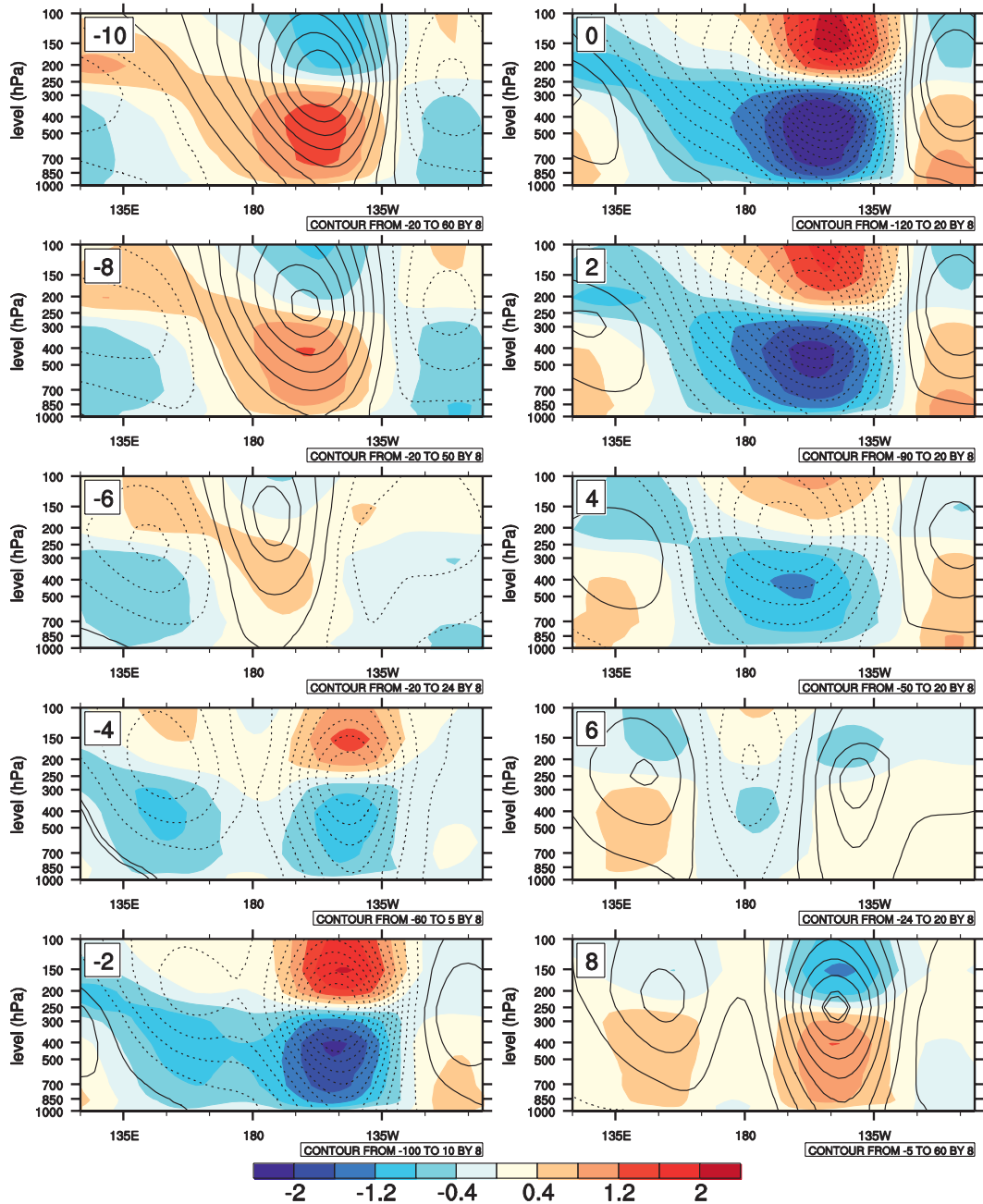


FIG. 5. Evolution of the longitudinal-vertical profile of 10–50-day filtered geopotential height fields (contour; m) and temperature fields (shading; K) averaged over the latitudes 45°–55°N from day –10 to day 8. The y axis is irregularly distributed.

indicating that the interaction between the summer mean flow and the ISO perturbation favors the energy transfer from the mean flow to the ISO perturbation in this region.

The term  $\overline{CK}_{iso}$  is given by the sum of the four terms on the right side of Eq. (5) and the box-averaged value of each term is shown in Table 2. The major contribution to  $\overline{CK}_{iso}$  is the third term [i.e.,  $-\overline{u'v'}(\partial\bar{u}/\partial y)$ ]. The horizontal

distributions of  $-\partial\bar{u}/\partial y$  and  $\overline{u'v'}$  are further examined (see Figs. 6b,c). Both terms are positive in the box region. This implies that both the mean zonal wind shear associated with the upper-troposphere jet and the northeast–southwest tilting of the ISO flow are responsible for the energy conversion from the mean flow to the ISO flow.

For comparison, we also calculate the barotropic energy conversion between the mean flow and the synoptic-scale

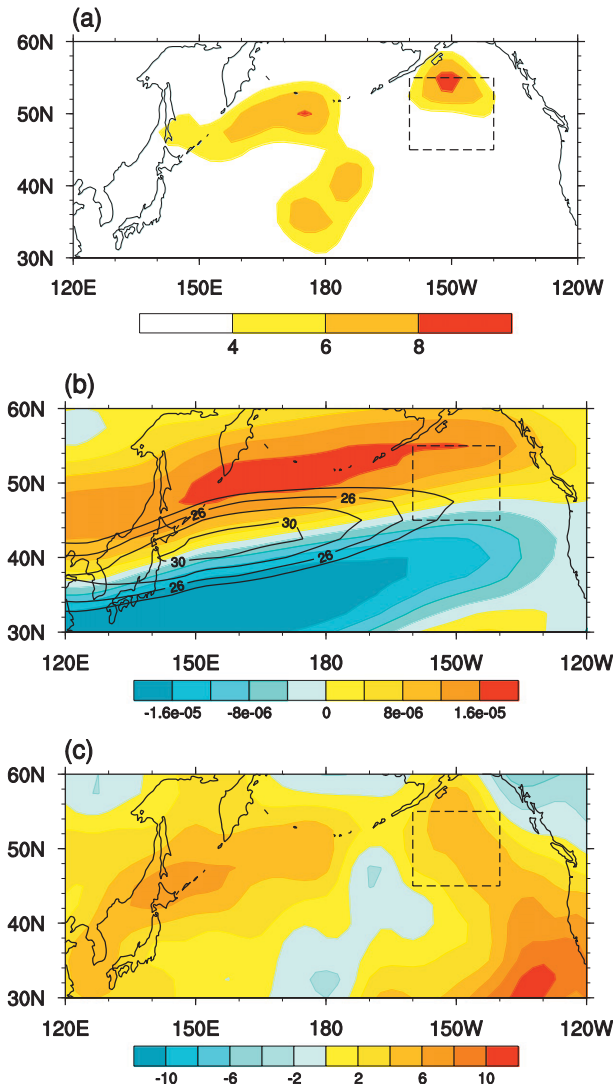


FIG. 6. Horizontal distribution of (a) ISO-related barotropic energy conversion  $\overline{\overline{CK}}_{iso}$  ( $10^{-5} \text{ m}^2 \text{ s}^{-3}$ ), (b)  $-\partial\bar{u}/\partial y$  (shaded;  $\text{s}^{-1}$ ) and  $\bar{u}$  (contour;  $\text{m s}^{-1}$ ), and (c)  $\overline{u'v'}$  ( $\text{m}^2 \text{ s}^{-2}$ ) at 250 hPa during boreal summer. The double overbar represents the summer mean component, and the prime represents the intraseasonal component.

perturbation ( $\overline{\overline{CK}}_{ssv}$ ) averaged in the same box. The results are shown in Table 3. The term  $\overline{\overline{CK}}_{ssv}$  is negative, which indicates that this is a region where energy transfers from the synoptic perturbation to the mean flow. If the ISO flow effect is included in the calculation of  $\overline{\overline{CK}}_{ssv}$ , the synoptic-scale perturbation (SSV) would lose energy to the background flow in the same region (not shown).

The above results indicate that in the westerly jet exit region the ISO receives energy from the mean flow while the synoptic-scale perturbation loses energy to the mean flow, similar to the results of Cai et al. (2006). A further decomposition of  $\overline{\overline{CK}}_{ssv}$  shows that its maximum contribution comes from the term

TABLE 2. Individual terms of  $\overline{\overline{CK}}_{iso}$  ( $10^{-5} \text{ m}^2 \text{ s}^{-3}$ ) averaged in the box of  $45^{\circ}$ – $55^{\circ}$ N,  $160^{\circ}$ – $140^{\circ}$ W, where  $CK1 = [(\overline{v'^2} - \overline{u'^2})/2](\partial\bar{u}/\partial x)$ ,  $CK2 = [(-\overline{v'^2} - \overline{u'^2})/2](\partial\bar{v}/\partial y)$ ,  $CK3 = -\overline{u'v'}(\partial\bar{u}/\partial y)$ , and  $CK4 = -\overline{u'v'}(\partial\bar{v}/\partial x)$ .

CK1	CK2	CK3	CK4
-0.17	-0.27	3.17	-0.09

$$-\frac{\overline{v'^2} - \overline{u'^2}}{2} \frac{\partial\bar{v}}{\partial y}$$

As the mean flow is the same for the intraseasonal and synoptic-scale perturbations, the difference between  $\overline{\overline{CK}}_{iso}$  and  $\overline{\overline{CK}}_{ssv}$  is attributed to the difference in perturbation wind speed, particularly perturbation meridional wind speed (not shown).

### b. Phase propagation

According to Rossby wave dynamics, the phase speed of a barotropic Rossby wave is written as (Holton 2004)

$$C_x = \frac{\omega}{k} = \bar{u} - \frac{\beta^*}{k^2 + l^2}, \quad (8)$$

where  $\bar{u}$  denotes the vertical averaged velocity of the zonal mean flow in boreal summer,  $\beta^*$  is an equivalent- $\beta$  parameter that represents a sum of the meridional gradient of planetary ( $\beta$ ) and mean relative vorticity ( $\partial\bar{\zeta}/\partial y$ ), and  $k$  and  $l$  denote the zonal and meridional wavenumber of the barotropic Rossby wave. With the use of the NCEP–DOE reanalysis data,  $\bar{u}$  is estimated to be  $13.2 \text{ m s}^{-1}$  ( $14.6 \text{ m s}^{-1}$ ) when one averages the summer mean zonal wind from 700 to 100 hPa (from 500 to 100 hPa) in the region of  $45^{\circ}$ – $55^{\circ}$ N,  $180^{\circ}$ – $120^{\circ}$ W. Here  $k$  is estimated using the half zonal wavelength of  $\psi'$  (Fig. 3). Note that a half zonal wavelength is around  $50^{\circ}$  in longitude in EOF1 (Fig. 3a) and  $40^{\circ}$  in longitude in EOF2 (Fig. 3b). Thus, an average of the two leads to a full zonal wavelength of roughly  $90^{\circ}$  in longitude. The meridional half wavelength is estimated to be  $40^{\circ}$  in latitude. Substituting  $\bar{u}$ ,  $k$ , and  $l$  in Eq. (8), we derive a westward phase speed of  $2.7 \text{ m s}^{-1}$  (with  $\bar{u} = 13.2 \text{ m s}^{-1}$ ) and  $1.9 \text{ m s}^{-1}$  (with  $\bar{u} = 14.6 \text{ m s}^{-1}$ ), both of which are close to the observed ISO propagation speed ( $2.4 \text{ m s}^{-1}$ ). The analysis above implies the Rossby wave nature of the ISO perturbation in midlatitudes.

TABLE 3. Individual terms of  $\overline{\overline{CK}}_{ssv}$  ( $10^{-5} \text{ m}^2 \text{ s}^{-3}$ ) averaged in the box of  $45^{\circ}$ – $55^{\circ}$ N,  $160^{\circ}$ – $140^{\circ}$ W, where  $CK1 = [(\overline{v'^2} - \overline{u'^2})/2](\partial\bar{u}/\partial x)$ ,  $CK2 = [(-\overline{v'^2} - \overline{u'^2})/2](\partial\bar{v}/\partial y)$ ,  $CK3 = -\overline{u'v'}(\partial\bar{u}/\partial y)$ , and  $CK4 = -\overline{u'v'}(\partial\bar{v}/\partial x)$ .

CK1	CK2	CK3	CK4
-4.29	-7.39	-0.73	-0.07

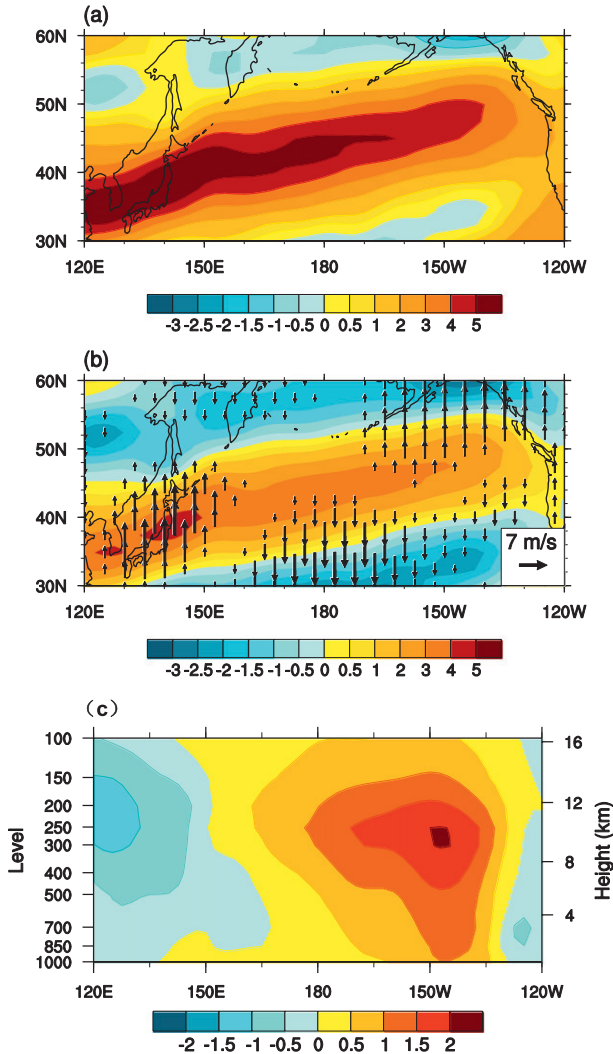


FIG. 7. Horizontal distribution of (a)  $\beta^*$  (shaded;  $10^{-11} \text{ m}^{-1} \text{ s}^{-1}$ ) at 250 hPa, and (b)  $\partial \bar{\zeta}' / \partial y$  (shaded;  $10^{-11} \text{ m}^{-1} \text{ s}^{-1}$ ) and summer mean meridional velocity (vector;  $\text{m s}^{-1}$ ) at 250 hPa. Note the irregular contour intervals in the color bar. (c) Longitudinal-vertical profile of  $\partial \bar{\zeta}' / \partial y$  ( $10^{-11} \text{ m}^{-1} \text{ s}^{-1}$ ) averaged along 45°–55°N. The double overbar represents the summer mean component. The y axis is irregularly distributed.

It is important to note that the local meridional gradient of mean relative vorticity plays an important role in promoting the westward phase propagation for the ISO. The horizontal and vertical distribution of  $\partial \bar{\zeta}' / \partial y$

(see Figs. 7b,c) shows that  $\partial \bar{\zeta}' / \partial y$  is positive and maximum in the region where the ISO perturbation moves westward. The averaged value of  $\partial \bar{\zeta}' / \partial y$  in the region is about one-half of  $\beta^*$  (see Fig. 7a). If the mean vorticity gradient were not present, the calculated phase speed for the ISO perturbation would be positive (see Table 4), implying that the ISO perturbation would propagate eastward.

For comparison, we also examine the propagation feature of the synoptic-scale perturbations and find that the average eastward speed is about  $8.3 \text{ m s}^{-1}$  (not shown). Substituting the horizontal scales of the synoptic perturbations, of which the zonal wavelength is about  $50^\circ$  in longitude (half of the ISO zonal wavelength) and the meridional wavelength is quite similar to that of the ISO perturbation, into Eq. (8), one can derive an eastward phase speed close to the observed propagation speed (not shown). Thus, the difference in the phase propagation characteristics between the ISO and the synoptic-scale perturbations is primarily attributed to the difference in their zonal scales. The propagation characteristics of both the synoptic and intraseasonal perturbations follow the barotropic Rossby wave dispersion relationship well [Eq. (8)].

### c. Growth mechanism for the ISO

Figure 8 shows the composite of intraseasonal vorticity anomalies at 250 hPa from day  $-6$  to day 2. The positive  $\zeta'$  slowly propagates westward and attains the maximum at day 0 at 150°W. It is consistent with the evolution of the negative intraseasonal streamfunction anomalies shown in Fig. 4. The evolution of the column-averaged  $[\zeta']$  following the cyclonic center (averaged in the boxes in Fig. 8) is shown as a solid line in Fig. 9, and the vorticity change rate ( $D[\zeta'] / Dt$ ) is shown as a dashed line. It is found that the maximum vorticity anomaly occurs at day 0, whereas the maximum positive vorticity tendency occurs at day  $-4$ .

The development of the ISO perturbation may be understood with a center-followed vorticity budget analysis. Figure 10a shows the observed  $D[\zeta'] / Dt$  and the contribution of each term in the budget Eqs. (1) and (2) at day  $-4$ . It is found that the sum of the right-hand-side terms in Eqs. (1) and (2) represents the observed tendency well and the residual is small. The positive vorticity tendency is primarily attributed to the meridional

TABLE 4. The mean zonal wind speed ( $\text{m s}^{-1}$ ), the mean vorticity gradient ( $\text{s}^{-1}$ ), and corresponding Rossby wave phase speeds of ISO perturbations ( $\text{m s}^{-1}$ ), averaged over the region of 45°–55°N, 180°–120°W, at different vertical depths.

Vertical depth	$\bar{u}$	$\partial \bar{\zeta}' / \partial y$	$C_x = \bar{u} - \frac{\beta^*}{k^2 + l^2}$	$C_x = \bar{u} - \frac{\beta}{k^2 + l^2}$
700–100 hPa	13.2	$8.3 \times 10^{-12}$	–2.7	3.0
500–100 hPa	14.6	$9.0 \times 10^{-12}$	–1.9	4.4

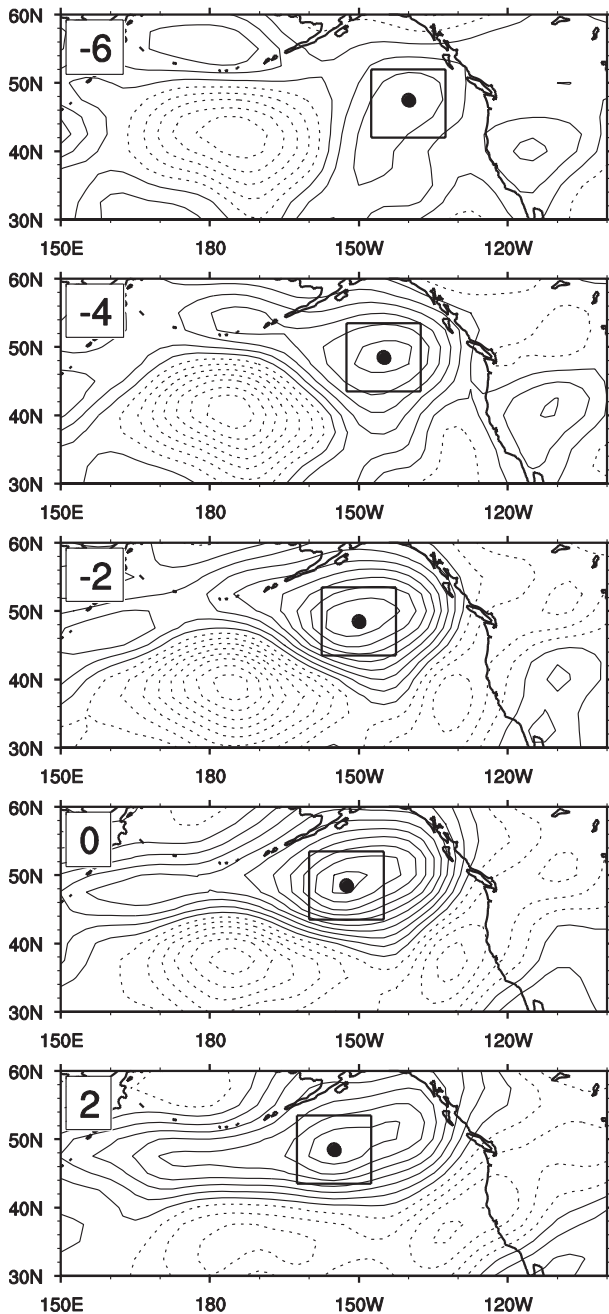


FIG. 8. Composite of 10–50-day filtered vorticity anomalies ( $2 \times 10^{-6} \text{ s}^{-1}$ ) at 250 hPa from day  $-6$  to day  $+2$  relative to EOF1 of the 10–50-day streamfunction anomalies. The dot represents the center of positive vorticity anomalies.

advection of relative vorticity  $[(-v\partial\zeta/\partial y)']$  and the other terms are relatively small.

How does the term  $[(-v\partial\zeta/\partial y)']$  contribute to the growth of the intraseasonal perturbation? To address this question, we further decompose each variable into three time scales as in Eq. (3) and consider the possible

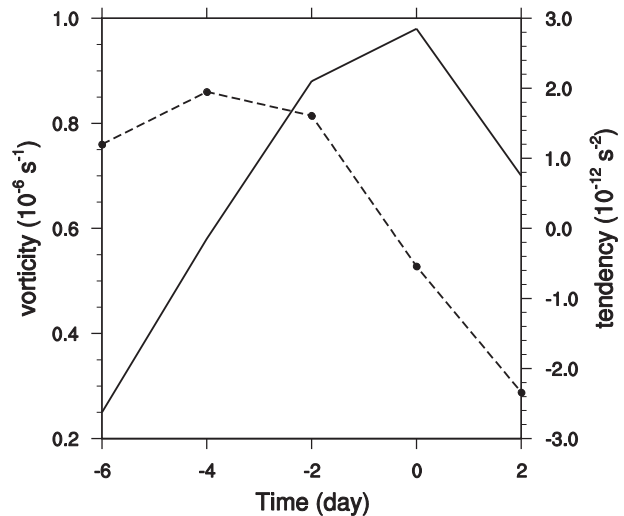


FIG. 9. The solid line indicates the composite of column-averaged intraseasonal vorticity anomalies  $[\zeta']$  ( $10^{-6} \text{ s}^{-1}$ ) averaged in the boxes marked in Fig. 8 from day  $-6$  to day  $+2$ . The dashed line is the same, but for the vorticity tendency  $D[\zeta']/Dt$  ( $10^{-12} \text{ s}^{-2}$ ).

influence of multiscale interaction. Figure 10b shows the contribution of each term in Eq. (4) at day  $-4$ . It is found that the leading term that contributes to the ISO growth is the meridional eddy vorticity transport term  $[(-v''\partial\zeta''/\partial y)']$ .

How does the synoptic eddy vorticity transport contribute to the growth of the intraseasonal perturbation? To address this question, we first examine the dominant pattern of the synoptic eddy in the developing phase of ISO cyclonic and anticyclonic vorticity anomalies in the region of interest (i.e., the northeastern Pacific). We first built two subdatasets for synoptic-scale perturbation field, one for ISO cyclonic vorticity background condition and the other for ISO anticyclonic vorticity background condition, both of which correspond to the time from day  $-8$  to day  $0$  in Fig. 4 but with an opposite sign of the streamfunction anomaly. Once the two subdatasets were built, we obtained a maximum synoptic-scale variability center in the region, regarded its time series as a reference time series, and regressed the synoptic eddy vorticity anomalies  $\zeta''$  at each grid point against the reference time series. The horizontal distributions of the regressed  $\zeta''$ , from day  $0$  to day  $+2$ , are shown in Fig. 11. It is interesting to note that the synoptic vorticity pattern is tilted toward the northwest–southeast (northeast–southwest) direction during the positive (negative)  $\zeta'$  growing phase. This suggests that the ISO plays a role in determining the eddy tilt structure.

Figure 12 illustrates the zonal distribution of the regressed  $v''$  and  $\partial\zeta''/\partial y$  averaged along  $45^{\circ}$ – $55^{\circ}$ N in the ISO developing region. During the positive  $\zeta'$  growing

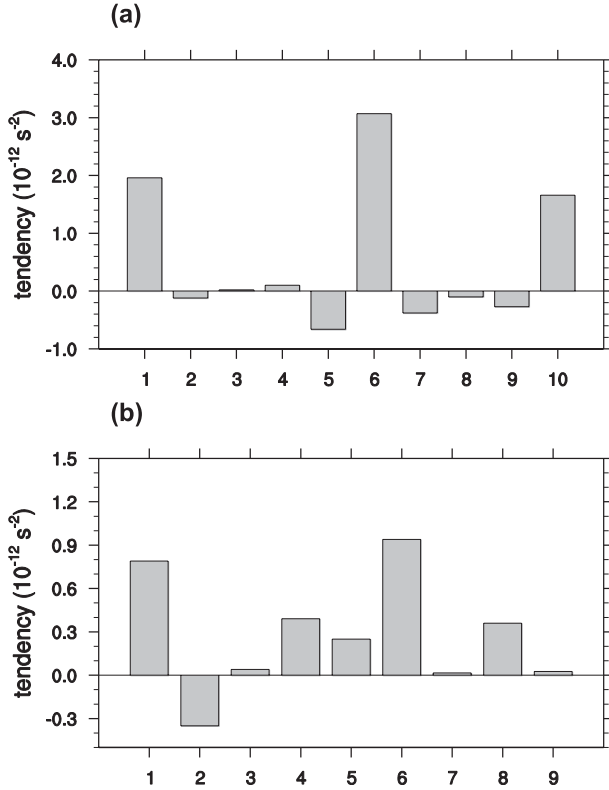


FIG. 10. (a) Individual intraseasonal vorticity tendency ( $10^{-12} \text{ s}^{-2}$ ) terms averaged at the center of the intraseasonal cyclonic anomalies (see the box in Fig. 8) for day -4 composite. The leftmost term on the x axis (bar 1) shows the observed tendency  $D[\zeta']/Dt$ , whereas the rightmost (bar 10) shows the sum of all budget terms  $\partial[\zeta']/\partial t + C_r \partial[\zeta']/\partial x$ . The remaining terms are bar 2:  $\{[-(\zeta + f)\nabla \cdot \mathbf{V}']\}$ , bar 3:  $\{[(\partial\omega/\partial y)(\partial u/\partial p)']\}$ , bar 4:  $\{-[(\partial\omega/\partial x)(\partial v/\partial p)']\}$ , bar 5:  $\{[-(u\partial\zeta'/\partial x)']\}$ , bar 6:  $\{[-(v\partial\zeta'/\partial y)']\}$ , bar 7:  $\{[-(\omega\partial\zeta'/\partial p)']\}$ , bar 8:  $\{-\beta v'\}$ , and bar 9:  $C_r \partial[\zeta']/\partial x$ . (b) Individual terms of  $[(-v\partial\zeta'/\partial y)']$  averaged at the center of the intraseasonal cyclonic anomalies (see the box) for day -4 composite, where bar 1 is  $[(-\bar{v}\partial\zeta'/\partial y)']$ , bar 2 is  $[(-v'\partial\zeta'/\partial y)']$ , bar 3 is  $[(-v'\partial\zeta'/\partial y)']$ , bar 4 is  $[(-v'\partial\zeta'/\partial y)']$ , bar 5 is  $[(-v'\partial\zeta'/\partial y)']$ , bar 6 is  $[(-v'\partial\zeta'/\partial y)']$ , bar 7 is  $[(-v'\partial\zeta'/\partial y)']$ , bar 8 is  $[(-\bar{v}\partial\zeta'/\partial y)']$ , and bar 9 is  $[(-v'\partial\zeta'/\partial y)']$ .

phase,  $v''$  and  $\partial\zeta''/\partial y$  are negatively correlated in most of the region, leading to a positive zonal mean value of  $-v''\partial\zeta''/\partial y$  (see the numbers on the upper right corner); during the negative  $\zeta'$  growing phase,  $v''$  and  $\partial\zeta''/\partial y$  are mostly positively correlated, leading to a negative zonal mean value of  $-v''\partial\zeta''/\partial y$  (see the numbers in the upper right corner). As a result, the eddy–eddy interaction  $-v''\partial\zeta''/\partial y$  contributes to the growth of the ISO vorticity regardless of its sign.

These results suggest a two-way interaction between the ISO and synoptic-scale flows. On one hand, the ISO controls the tilting of synoptic-scale eddies. On the other, the tilted synoptic-scale eddies strengthen the ISO perturbation through eddy vorticity transport. It is noted that the modulation of the eddy tilting structure

by the ISO vorticity is similar to the modulation of the upper-troposphere breaking waves by the meridional shift of the jet axis proposed by previous studies (e.g., Moore et al. 2010). The upscale feedback mechanism can be further illustrated by a schematic diagram shown in Fig. 13. Under the ISO cyclonic flow, the trough of the synoptic eddy (see the dashed line in Fig. 13a) is tilted toward the northwest–southeast direction. To the west of the trough (shaded region in Fig. 13a), the meridional wind anomaly is southward ( $v'' < 0$ ) and the meridional gradient of the vorticity anomaly is positive ( $\partial\zeta''/\partial y > 0$ ). To the east of the trough (white region in Fig. 13a), the meridional wind anomaly is northward ( $v'' > 0$ ) and the meridional gradient of the vorticity anomaly is negative ( $\partial\zeta''/\partial y < 0$ ). As a result,  $-v''\partial\zeta''/\partial y$  is greater than zero (i.e., cyclonic eddy vorticity transport) in both regions, so that it contributes to the growth of the intraseasonal cyclonic anomaly. Similarly, under the ISO anticyclonic flow, the trough of the synoptic eddy (see the dashed line in Fig. 13b) is tilted toward the northeast–southwest direction. To the west of the trough (white region in Fig. 13b), the meridional wind anomaly is southward ( $v'' < 0$ ) and the meridional gradient of the vorticity anomaly is negative ( $\partial\zeta''/\partial y < 0$ ), whereas to the east of the trough (shaded region in Fig. 13b), the meridional wind anomaly is northward ( $v'' > 0$ ) and the meridional gradient of the vorticity anomaly is positive ( $\partial\zeta''/\partial y > 0$ ). As a result,  $-v''\partial\zeta''/\partial y$  is less than zero and it contributes to the growth of the intraseasonal anticyclonic anomaly. This positive feedback process is consistent with that proposed recently by Jin (2010).

The second leading term in the anomalous meridional vorticity advection (Fig. 10b) is  $[(-\bar{v}\partial\zeta'/\partial y)']$ . This term represents the effect of the ISO–mean flow interaction. As the mean meridional velocity is northward in the ISO developing region (near  $50^\circ\text{N}$ ; see vectors in Fig. 7b) and the maximum value appears to the north of the ISO center, the area-averaged meridional advection of the anomalous cyclonic (anticyclonic) vorticity by the mean wind ( $-\bar{v}\partial\zeta'/\partial y$ ) is positive (negative). This helps the meridional expansion of the intraseasonal cyclonic (anticyclonic) perturbation.

#### d. Initiation of ISO perturbations

It was shown in Fig. 4 that the westward-propagating ISO originates from the region around  $120^\circ\text{W}$  (at day -10 or day -8). Why is there an initial ISO perturbation near  $120^\circ\text{W}$ ? To reveal the perturbation source region, a wave-activity flux (Takaya and Nakamura 2001) is calculated for the ISO flow at 250 hPa. Figure 14 shows the horizontal distributions of the wave activity flux and the flux divergence fields. While pronounced eastward wave activity fluxes appear along the midlatitude

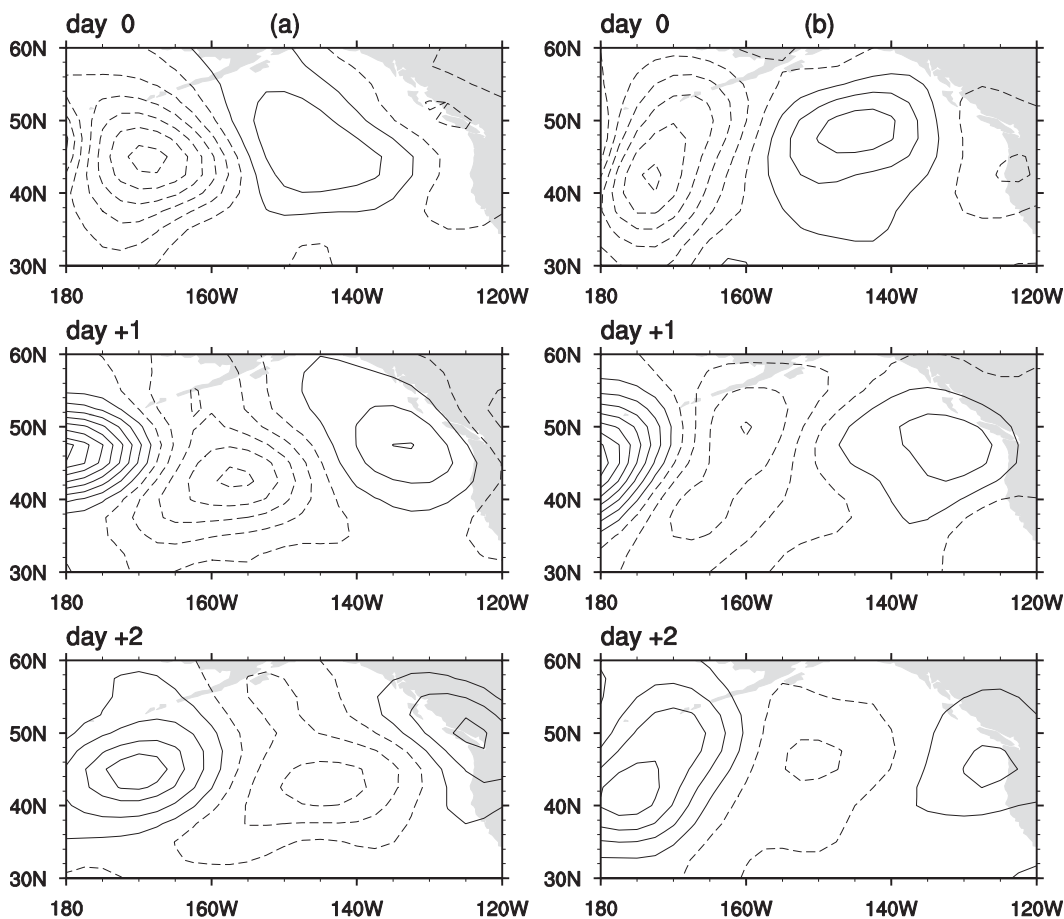


FIG. 11. (a) Regressed synoptic-scale vorticity fields ( $s^{-1}$ ; interval  $0.3 \times 10^{-5} s^{-1}$ ) during the developing phase of an ISO cyclonic perturbation. (b) As in (a), but during the developing phase of an ISO anticyclonic perturbation.

upper-level westerly, a flux convergence is found near  $120^{\circ}W$ . This indicates that, although its phase propagates westward, the ISO emits wave energy eastward, and the wave energy is accumulated near  $120^{\circ}W$ . The energy accumulation is hypothesized to be a major process that triggers and initiates the initial ISO signal. This hypothesis, however, needs further verification.

### 5. Relative contribution of tropical forcing and local processes

The diagnosis results above suggest that the midlatitude ISO may initiate, grow, and self-maintain through internal atmospheric dynamics. This is in contrast to a tropical forcing scenario in which tropical convection associated with MJO may remotely trigger and maintain the midlatitude ISO. Thus, an open question is: What is the relative contribution of the remote tropical forcing and local processes to the midlatitude ISO? To address this question, we take both the observational analysis and idealized numerical modeling approaches.

#### a. Reanalysis data diagnosis

In this subsection, the NCEP–DOE reanalysis data are used to explore the impacts of the tropical intra-seasonal variability. Both of the time series of PC1 and PC2 (hereafter RMM1 and RMM2) retrieved by the multivariate (MV)-EOF analysis on 10–90-day filtered 200-hPa zonal wind (U200), 850-hPa zonal wind (U850), and OLR (Liebmann and Smith 1996) averaged between  $15^{\circ}S$  and  $15^{\circ}N$  (Wheeler and Hendon 2004) are used to represent the MJO forcing. As the average period of an MJO case is about 45 days, an averaged time interval between each of the eight MJO phases is about 6 days. According to the definition of eight MJO phases in Wheeler and Hendon (2004), the maximum values of RMM1 are between phases 4 and 5, and the maximum values of RMM2 are between phases 6 and 7. So, the 3-day-lead regression field of a variable (VAR) against the RMM1 time series represents the phase-4 average situation of VAR, and the 3-day-lag regression field of VAR against the RMM1 time series represents the

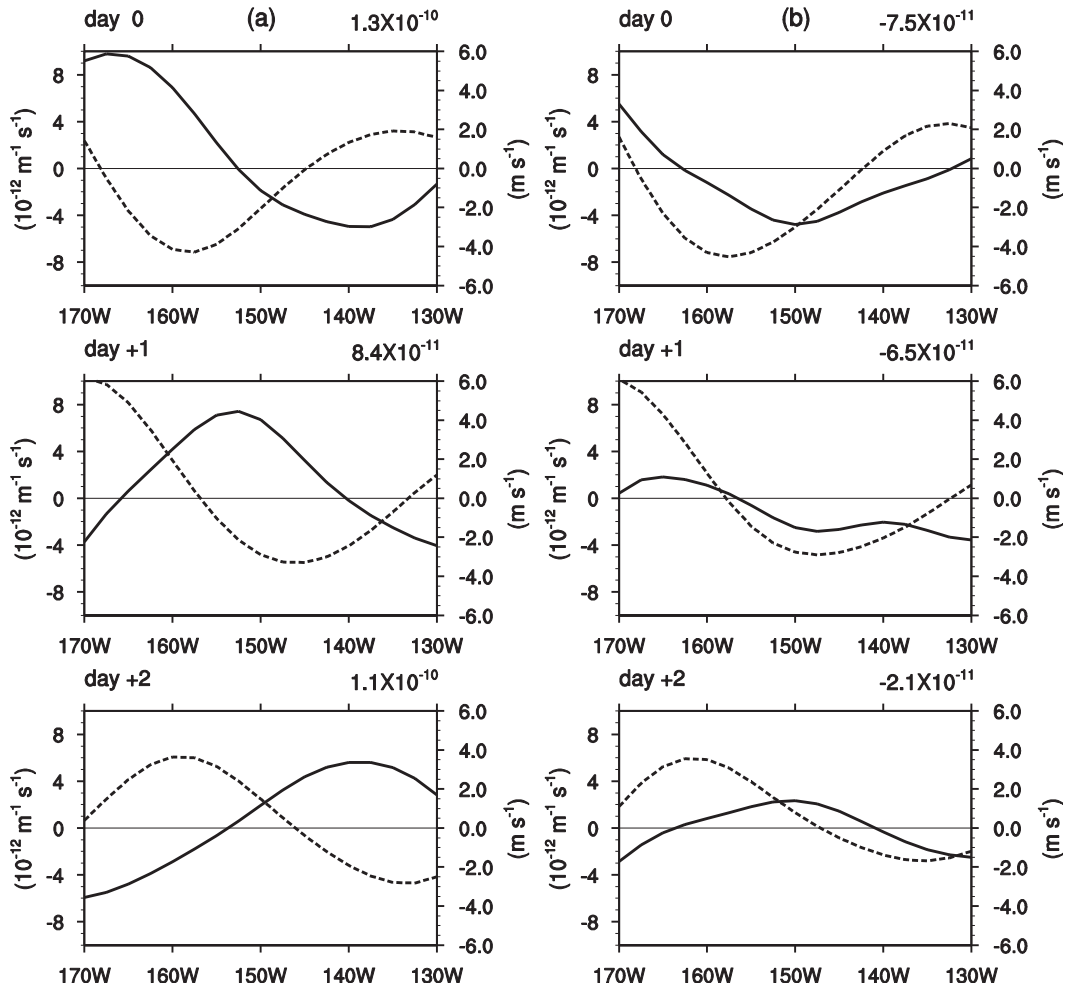


FIG. 12. (a) Regressed synoptic meridional wind anomalies ( $v''$ , dashed line;  $\text{m s}^{-1}$ ) and meridional gradient of synoptic vorticity anomalies ( $\partial\zeta''/\partial y$ , solid line;  $10^{-12} \text{ m}^{-1} \text{ s}^{-1}$ ) averaged along  $45^\circ\text{--}55^\circ\text{N}$  during the developing phase of an ISO cyclonic perturbation. (b) As in (a), but during the developing phase of an ISO anticyclonic perturbation. Number in the upper-right corner of each panel denotes the zonally integrated values of  $-v''\partial\zeta''/\partial y$ .

phase-5 average situation of VAR. Likewise, the 3-day-lead (lag) regression field of VAR against the RMM2 time series represents the phase-6 (7) average situation of VAR. As phases 1 (2) and 8 (3) are opposite to phases 5 (6) and 4 (7), respectively, the average situations of VAR from phase 8 to phase 1 can also be obtained. Multiplying the regression field in each phase by the corresponding PC time series would result in the time-varying fields of VAR (VAR') in each phase. Furthermore, the standard deviation of the so-calculated intraseasonal VAR' in each phase represents the MJO forcing effect. The ratio of this to the standard deviation of the total ISO signal represents the fractional contribution of the MJO forcing.

As the RMM time series include not only the strong MJO cases but also the weak MJO cases and the non-MJO cases, if all times of RMM1 and RMM2 were used,

the impact of the MJO forcing might be underestimated. Therefore, we conduct additional calculations by examining only strong MJO cases through constructing strong MJO time series based on RMM1 and RMM2, and we compare the all-times result and the strong MJO result. Given a normalized time series, strong positive MJO cases are defined when its peak is above  $1.1\sigma$  and its minimum is below  $-1.1\sigma$ . Others are defined as weak cases. Only strong MJO cases are used to construct a new RMM time series (termed RMM\*) (see red curve in Fig. 15 as an example). The dominant period of the RMM\* time series is the same as that of the RMM time series (not shown).

Figure 16 shows the regression fields of 10–90-day filtered OLR and U200 in different phases of MJO based on RMM1\* and RMM2\*. In phase 1, U200 fields have a Gill–Matsuno-type (Gill 1980) response in the

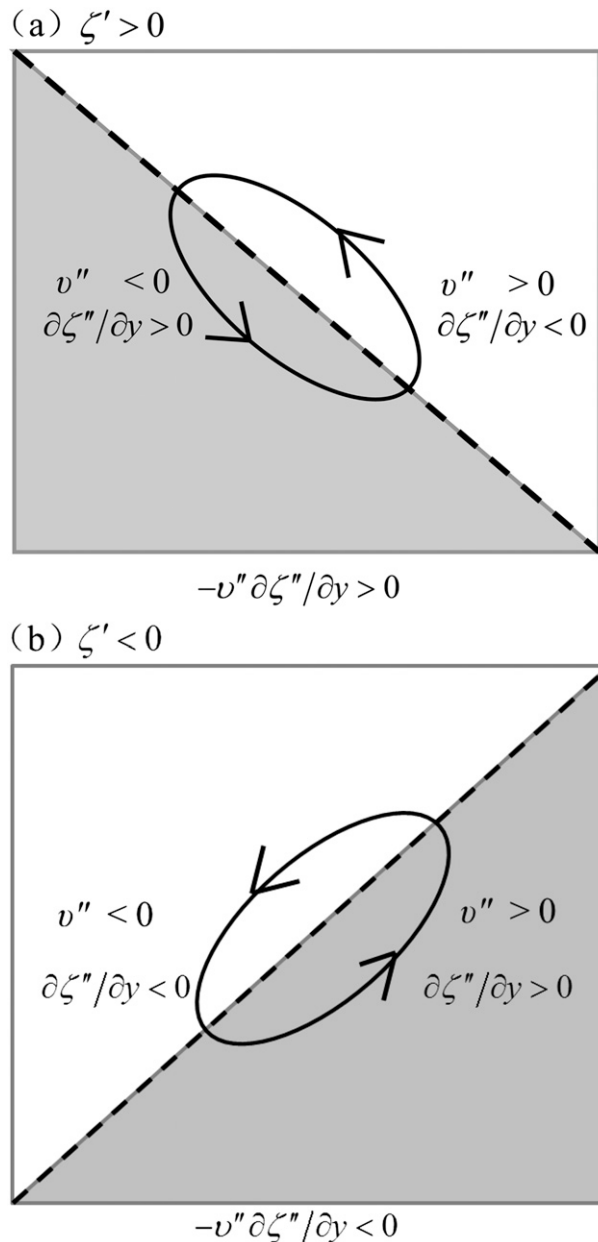


FIG. 13. Schematic diagram illustrating a positive feedback between the ISO and synoptic-scale flows during the developing phase of (a) an ISO cyclonic perturbation and (b) an ISO anticyclonic perturbation. The dashed line represents the trough of a synoptic eddy.

tropics to the suppressed convection over the Maritime Continent and some teleconnection patterns in the midlatitudes. The response signals change as the convective anomalies move eastward. The response patterns from phase 5 to 8 are opposite to those from phase 1 to 4. Figure 17 shows the horizontal distribution of the standard deviation of  $U200'$  at each phase. The maximum

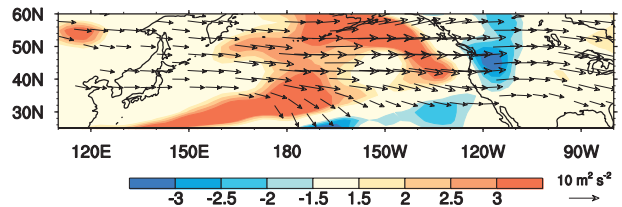


FIG. 14. Horizontal distribution of wave-activity flux (vector;  $\text{m}^2 \text{s}^{-2}$ ) and divergence (shading;  $10^{-6} \text{s}^{-1}$ ) at 250 hPa averaged in boreal summer. The vectors with the scales less than  $5 \text{m}^2 \text{s}^{-2}$  are omitted.

intraseasonal variability in  $U200$  appears in the tropical region and decreases with latitude.

The maximum fractional contribution in  $U200$  based on the strong MJO cases is shown in Fig. 18a. It is found that the maximum MJO contribution to the midlatitude intraseasonal  $U200$  is about 20%–25% over the midlatitude North Pacific region. The maximum MJO contribution to the intraseasonal  $H200$  is also over the midlatitude North Pacific region and is about 20%–25% (see Fig. 18b). Furthermore, the maximum MJO contribution averaged in midlatitudes over the Northern Hemisphere ( $30^\circ$ – $60^\circ\text{N}$ ,  $0^\circ$ – $360^\circ$ ) is about 10% (see Table 5). In the analysis above, we focused on tropical MJO events whose amplitudes are greater than  $1.1\sigma$ . We also conducted a sensitivity test by considering MJO events that are greater than  $1.5\sigma$  or even  $2\sigma$ . It turns out that the response patterns are almost identical (not shown), with the amplitude increasing by about 10% (see Table 5).

For comparison, the maximum fractional contributions based on all-time RMM time series are shown in Figs. 18c and 18d. The patterns are quite similar to those derived from the strong MJO cases, but the magnitudes are smaller.

#### b. Diagnosis of numerical model experiments

The relative roles of tropical forcing and midlatitude processes based on idealized ECHAM4 experiments are assessed in this subsection. Figure 19 shows the zonal mean

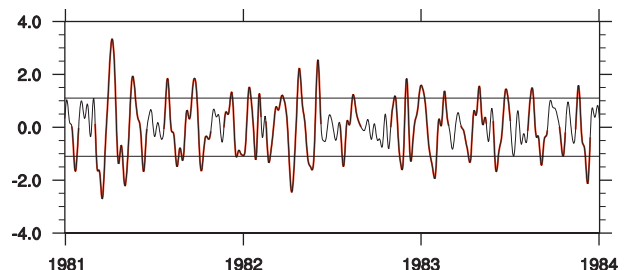


FIG. 15. Part of RMM1 time series retrieved by MV-EOF analysis on 10–90-day filtered 200-hPa zonal wind ( $U200$ ), 850-hPa zonal wind ( $U850$ ), and OLR during 1979–2009. The red curves represent the strong MJO cases used to construct RMM1\*.

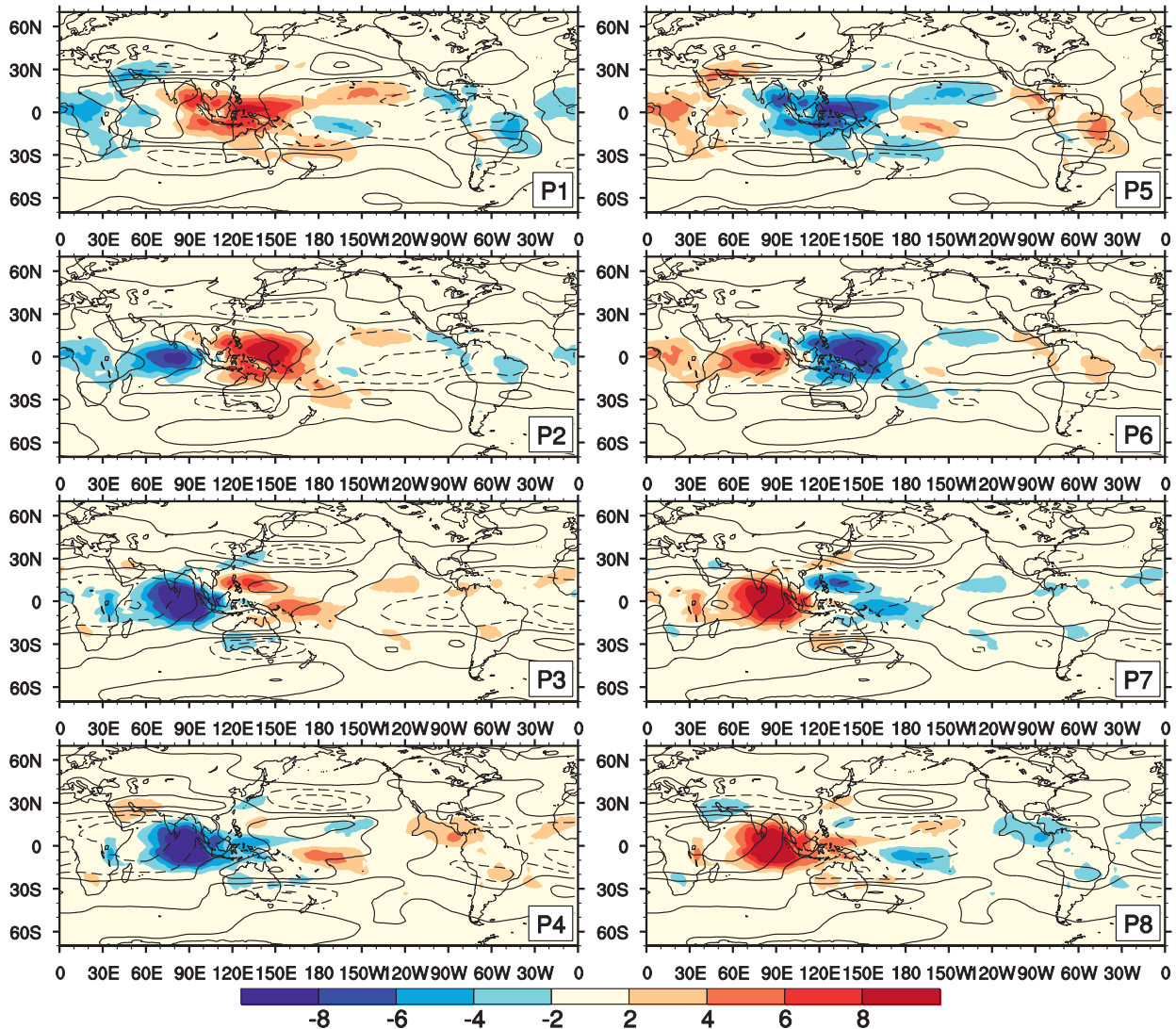


FIG. 16. Regression fields of the 10–90-day filtered OLR (shaded;  $\text{W m}^{-2}$ ) and 200-hPa zonal wind (contour;  $\text{m s}^{-1}$ ) anomalies at different MJO phases (marked in the bottom right of each panel) based on the strong MJO cases.

standard deviation of 10–90-day filtered H200 and U200 calculated from the NCEP–DOE reanalysis data and various numerical experiments. The patterns of ISO variability in the Control experiment are quite similar to those of the reanalysis data, except that the magnitudes are overestimated. In No\_Trop run, the amplitude of H200 is reduced compared to the Control run, implying the effect of tropical damping. With either a reduced damping rate or a smaller latitudinal extent of damping (i.e., Damp\_Sensitivity or Lat\_Sensitivity run), the amplitude of the intraseasonal oscillation in midlatitudes is stronger than in the No\_Trop run but weaker than in the Control run.

To quantitatively measure the change of midlatitude ISO, we introduce the following index that measures the ratio of the amplitude change of midlatitude ISO:

$$[\sigma(\text{VAR}_{\text{EXP}}) - \sigma(\text{VAR}_{\text{Control}})] / \sigma(\text{VAR}_{\text{Control}}), \quad (9)$$

where  $\sigma$  is the standard deviation, VAR represents any given 10–90-day filtered variable (e.g., H200 or U200) and EXP represents the experiment name.

Table 6 shows the ratio of the tropical forcing defined as in Eq. (9) averaged in midlatitudes over Northern Hemisphere. The No\_Trop run shows that the amplitude of the 10–90-day filtered H200 and U200 would be reduced by about 20% in the midlatitudes compared to the Control run. With a fourfold reduction of the damping rate and a decrease of the damping region, the reduction rate is less, as more tropical ISO variability is retained. Therefore, the results of the No\_Trop run are sensitive to the damping rate and the damping domain. The additional sensitivity

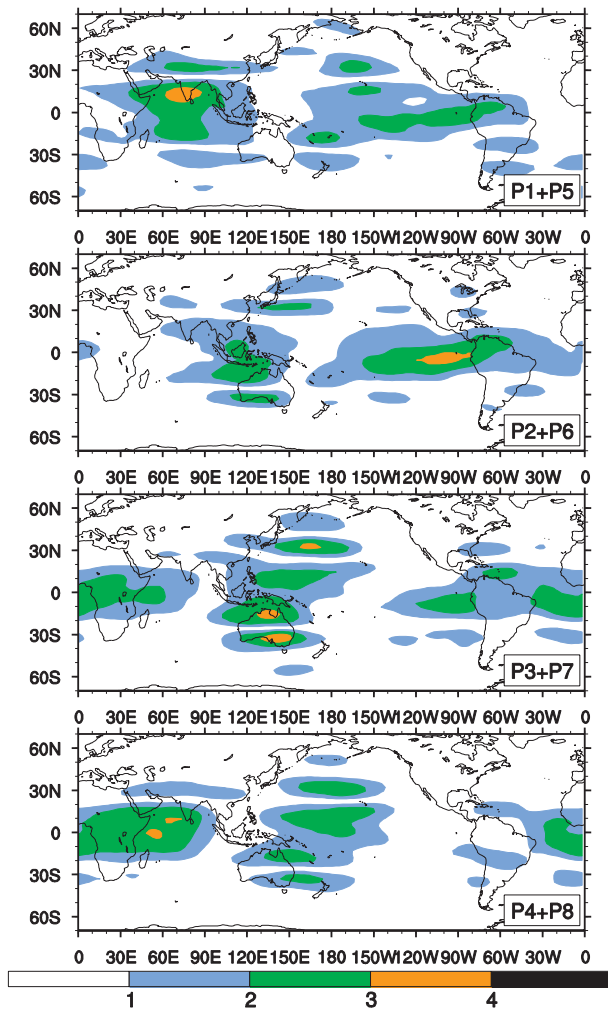


FIG. 17. Standard deviations of 10–90-day filtered 200-hPa zonal wind anomalies ( $\text{m s}^{-1}$ ) at each opposite pair of the MJO phases (marked in the bottom right of each panel), which are reconstructed by multiplying the regression fields with RMM\*.

experiments suggest that strong damping is needed to fully assess the tropical impact on midlatitude ISO.

Thus, both the observational data analysis and the idealized numerical experiments suggest that the primary source for the midlatitude ISO arises from local processes. The contribution of tropical forcing to the midlatitude ISO is about 20%. However, caution is needed when interpreting the results above, because in the observational analysis the Wheeler–Hendon index was used, which can only represent a part of the total tropical ISO variability, and in the ECHAM sensitivity experiment the tropical ISO is not fully suppressed.

## 6. Conclusions and discussion

The three-dimensional structural and evolutionary characteristics of the ISO over the midlatitude North

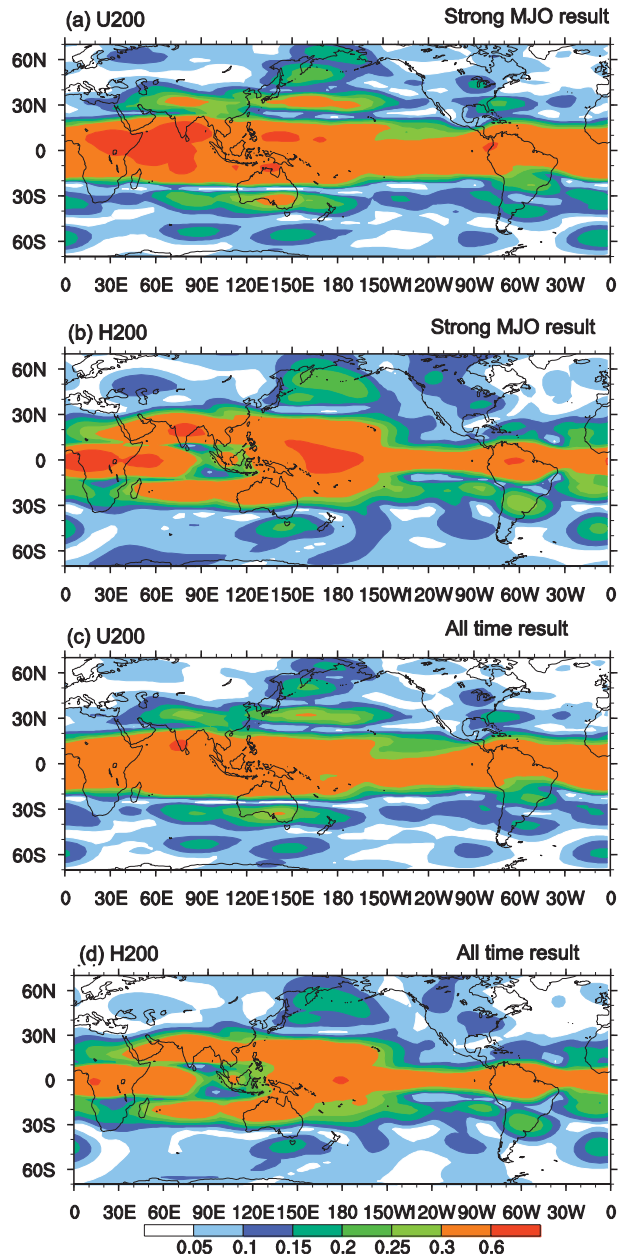


FIG. 18. (a) Maximum ratio of the MJO-induced variability to the total intraseasonal variability of zonal wind at 200 hPa, calculated based on strong MJO cases. (b) As in (a), but for the geopotential height at 200 hPa. (c),(d) As in (a),(b), but the calculations were based on all-time results.

Pacific Ocean during boreal summer were examined by diagnosing the NCEP–DOE reanalysis data. An EOF analysis reveals that the midlatitude ISO has an equivalent-barotropic structure and propagates westward with a typical zonal wavelength of about  $90^\circ$ . The maximum amplitude appears in the upper troposphere around 250 hPa. The temperature anomaly is in the hydrostatic

TABLE 5. Maximum ratio (%) of the MJO-induced variability to the total intraseasonal variability of 200-hPa geopotential height (H200) and 200-hPa zonal wind (U200) averaged over the Northern Hemisphere (30°–60°N, 0°–360°), calculated for strong MJO cases according to different criteria.

Criteria	H200	U200
1.1 $\sigma$	10	11
1.5 $\sigma$	12	13
2 $\sigma$	16	18

relation with the geopotential height anomaly, with a warm core above and a cold core below a negative height center. While the vorticity or streamfunction anomaly is co-located with the height anomaly, the vertical motion has a 90° phase difference with the vorticity field, with anomalous ascending motion appearing to the east of a cyclonic vorticity center.

The maximum ISO variability appears over the eastern North Pacific around 50°N, 150°W. Maximum positive barotropic energy conversion occurs in the maximum ISO activity region, indicating that the energy source for the ISO perturbation comes from the mean flow. The ISO perturbation appears initiated around 120°W, where wave activity fluxes converge.

The westward phase speed is determined by the column-averaged mean zonal wind, equivalent- $\beta$  effect, and the zonal wavelength of the ISO perturbations, as confirmed by the barotropic Rossby wave dispersion relation. In addition to the meridional gradient of planetary vorticity, the meridional gradient of relative vorticity of the mean flow also plays an important role in promoting the westward propagation.

The center-followed vorticity budget shows that the growth of the ISO vorticity perturbation is primarily attributed to the nonlinear meridional eddy vorticity transport. A two-way interaction scenario was identified for the ISO and synoptic-scale flows. On one hand, a cyclonic or anticyclonic ISO flow causes the synoptic-scale eddy to tilt along the northwest–southeast or northeast–southwest direction. On the other hand, the tilted synoptic eddies exert an upscale feedback to reinforce the ISO cyclonic or anticyclonic flows through nonlinear eddy vorticity transport.

The relative roles of the remote tropical forcing versus the midlatitude internal dynamics are investigated based on the diagnosis of both the observational data and idealized numerical experiments. By considering the impact of strong MJO events, the so-calculated ISO variability in midlatitudes occupies only about 20% of total intraseasonal variability at most, and this is consistent with numerical experiments, which shows that while the tropical MJO is greatly suppressed, a large portion of midlatitude intraseasonal variability is still present. This suggests that

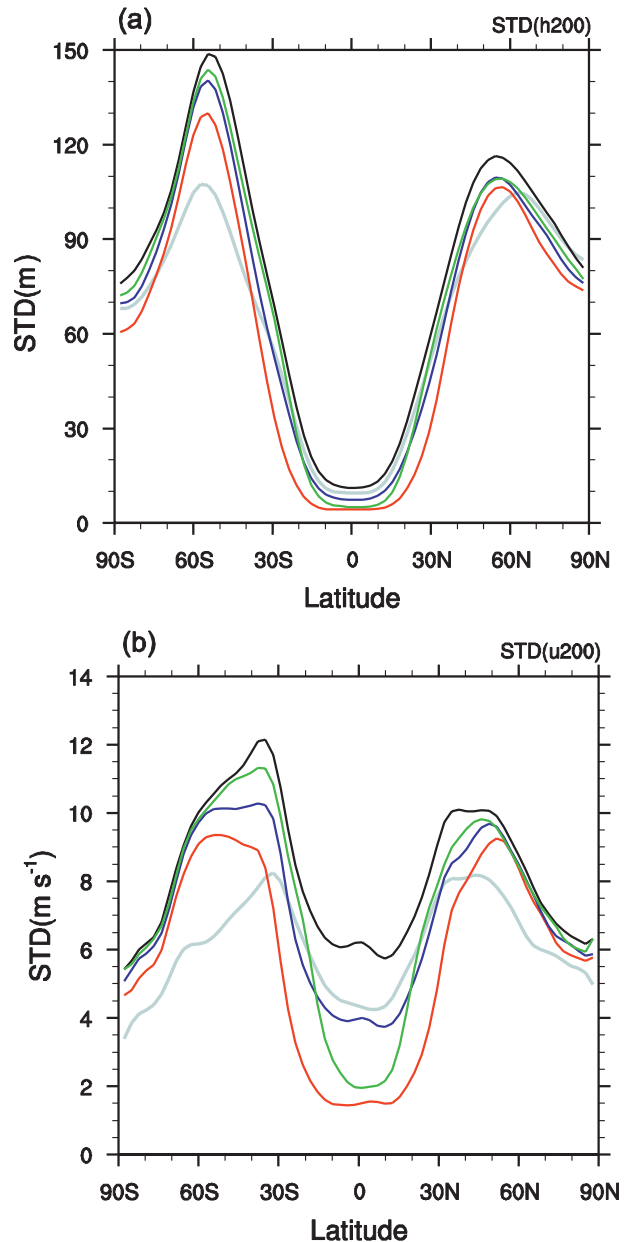


FIG. 19. (a) Zonal mean standard deviation of 10–90-day filtered 200-hPa geopotential height anomalies based on NCEP–DOE reanalysis data (gray line), the Control run (black line), the No\_Trop run (red line), the Damp\_Sensitivity run (blue line), and the Lat\_Sensitivity run (green line) for the whole year. (b) As in (a), but for the 200-hPa zonal wind anomalies.

the large amount of midlatitude intraseasonal variability arises from local internal dynamic processes, as pointed out in section 4. Whereas the initiation arises from energy accumulation associated with wave activity flux convergence, the amplification results from both barotropic energy conversion of the mean flow and a positive feedback between the ISO flow and eddy vorticity transport.

TABLE 6. Fractional contribution (%) of tropical intraseasonal signals to the magnitude of the 10–90-day filtered 200-hPa geopotential height anomalies (H200) and 200-hPa zonal wind anomalies (U200) in Northern Hemisphere (30°–60°N, 0°–360°) for the whole year.

	H200	U200
No_Trop run	18	15
New_Damp run	10	8
New_Latitude run	7	5

However, it is likely that the methodology applied in this paper may underestimate the tropical impact. First, the Wheeler–Hendon index represents only part of the intraseasonal signals in the tropics. As the result, the tropical forcing effect may be underestimated. Second, sensitivity experiments such as the No\_Trop run do not completely eliminate the MJO signal in the tropics. The simplistic measure of the standard deviation from the two model simulations may not be able to address the issue of cause and effect. It is likely that at least in some cases the tropical forcing is crucial. Once initiated by tropical forcing, a midlatitude perturbation may be further amplified through internal atmospheric dynamics (e.g., Mori and Watanabe 2008; Franzke et al. 2011). In such a scenario, the tropical forcing might appear small given the methodology employed here, but in reality it is of primary importance.

*Acknowledgments.* This work was supported by NSFC (Grant 41125017), China R&D Special Fund for Public Welfare Industry (meteorology) (GYHY200806010), NSF Grant AGS-1106536, NOAA Grant NA11OAR4310087, ONR Grant N000141210450, and by the International Pacific Research Center, which is sponsored by the Japan Agency for Marine–Earth Science and Technology (JAMSTEC), NASA (NNX07AG53G), and NOAA (NA17RJ1230).

#### REFERENCES

- Cai, M., S. Yang, H. M. van den Dool, and V. E. Kousky, 2006: Dynamical implications of the orientation of atmospheric eddies: A local energetic perspective. *Tellus*, **59A**, 127–140, doi:10.1111/j.1600-0870.2006.00213.x.
- Chen, T.-C., and M.-C. Yen, 1991: Interaction between intraseasonal oscillations of the midlatitude flow and tropical convection during 1979 northern summer: The Pacific Ocean. *J. Climate*, **4**, 653–671.
- Chen, W., 1982: Fluctuations in Northern Hemisphere 700-mb height field associated with the Southern Oscillation. *Mon. Wea. Rev.*, **110**, 808–823.
- Duchon, C., 1979: Lanczos filtering in one and two dimensions. *J. Appl. Meteor.*, **18**, 1016–1022.
- Franzke, C., S. B. Feldstein, and Coauthors, 2011: Synoptic analysis of the Pacific–North American teleconnection pattern. *Quart. J. Roy. Meteor. Soc.*, **137**, 329–346.
- Fu, X., and B. Wang, 2009: Critical roles of the stratiform rainfall in sustaining the Madden–Julian oscillation: GCM experiments. *J. Climate*, **22**, 3939–3959.
- Ghil, M., and K. Mo, 1991: Intraseasonal oscillations in the global atmosphere. Part I: Northern Hemisphere and tropics. *J. Atmos. Sci.*, **48**, 752–779.
- Gill, A. E., 1980: Some simple solutions for heat-induced tropical circulation. *Quart. J. Roy. Meteor. Soc.*, **106**, 447–462.
- Hendon, H. H., and M. L. Salby, 1994: The life cycle of the Madden–Julian oscillation. *J. Atmos. Sci.*, **51**, 2225–2225.
- Holton, J. R., 2004: *Introduction to Dynamic Meteorology*. Academic Press, 535 pp.
- Hoskins, B. J., I. N. James, and G. H. White, 1983: The shape, propagation and mean-flow interaction of large-scale weather systems. *J. Atmos. Sci.*, **40**, 1595–1612.
- Hsu, P.-C., and T. Li, 2012: Role of the boundary layer moisture asymmetry in causing the eastward propagation of the Madden–Julian oscillation. *J. Climate*, **25**, 4914–4931.
- Jiang, X., and N.-C. Lau, 2008: Intraseasonal teleconnection between the North American and western North Pacific monsoons with a 20-day time scale. *J. Climate*, **21**, 2664–2679.
- , T. Li, and B. Wang, 2004: Structures and mechanisms of the northward propagating boreal summer intraseasonal oscillation. *J. Climate*, **17**, 1022–1039.
- Jin, F.-F., 2010: Eddy-induced instability for low-frequency variability. *J. Atmos. Sci.*, **67**, 1947–1964.
- Kanamitsu, M., W. Ebisuzaki, J. Woollen, S.-K. Yang, J. J. Hnilo, M. Fiorino, and G. L. Potter, 2002: NCEP–DOE AMIP-II Reanalysis (R-2). *Bull. Amer. Meteor. Soc.*, **83**, 1631–1643.
- Kawamura, R., T. Murakami, and B. Wang, 1996: Tropical and midlatitude 45-day perturbations over the western Pacific during the northern summer. *J. Meteor. Soc. Japan*, **74**, 867–890.
- Knutson, T., and K. Weickmann, 1987: 30–60 day atmospheric oscillations—Composite life cycles of convection and circulation anomalies. *Mon. Wea. Rev.*, **115**, 1407–1436.
- Krishnamurti, T., and S. Gadgil, 1985: On the structure of the 30 to 50 day mode over the globe during FGGE. *Tellus*, **37A**, 336–360.
- Lau, K.-M., and T. J. Phillips, 1986: Coherent fluctuations of extratropical geopotential height and tropical convection in intraseasonal time scales. *J. Atmos. Sci.*, **43**, 1164–1181.
- , and L. Peng, 1987: Origin of low-frequency (intraseasonal) oscillations in the tropical atmosphere. Part I: Basic theory. *J. Atmos. Sci.*, **44**, 950–972.
- Li, T., and B. Wang, 1994: A thermodynamic equilibrium climate model for monthly mean surface winds and precipitation over the tropical Pacific. *J. Atmos. Sci.*, **51**, 1372–1385.
- , and C. Zhou, 2009: Planetary-scale selection of the Madden–Julian oscillation. *J. Atmos. Sci.*, **66**, 2429–2443.
- Liebmann, B., and D. L. Hartmann, 1984: An observational study of tropical–midlatitude interaction on intraseasonal time scales during winter. *J. Atmos. Sci.*, **41**, 3333–3350.
- , and C. A. Smith, 1996: Description of a complete (interpolated) outgoing longwave radiation dataset. *Bull. Amer. Meteor. Soc.*, **77**, 1275–1277.
- Madden, R. A., and P. R. Julian, 1971: Detection of a 40–50 day oscillation in the zonal wind in the tropical Pacific. *J. Atmos. Sci.*, **28**, 702–708.
- , and —, 1972: Description of global-scale circulation cells in the tropics with a 40–50 day period. *J. Atmos. Sci.*, **29**, 1109–1123.
- , and —, 1994: Observations of the 40–50-day tropical oscillation—A review. *Mon. Wea. Rev.*, **122**, 814–837.
- Maloney, E. D., 2009: The moist static energy budget of a composite tropical intraseasonal oscillation in a climate model. *J. Climate*, **22**, 711–729.

- Moore, R. W., O. Martius, and T. Spengler, 2010: The modulation of the subtropical and extratropical atmosphere in the Pacific basin in response to the Madden–Julian oscillation. *Mon. Wea. Rev.*, **138**, 2761–2779.
- Mori, M., and M. Watanabe, 2008: The growth and triggering mechanisms of the PNA: A MJO–PNA coherence. *J. Meteor. Soc. Japan*, **86**, 213–236.
- North, G., T. Bell, R. Cahalan, and F. Moeng, 1982: Sampling errors in the estimation of empirical orthogonal functions. *Mon. Wea. Rev.*, **110**, 699–706.
- Pan, L.-L., and T. Li, 2008: Interactions between the tropical ISO and midlatitude low-frequency flow. *Climate Dyn.*, **31**, 375–388.
- Rayner, N. A., D. E. Parker, E. B. Horton, C. K. Folland, L. V. Alexander, D. P. Rowell, E. C. Kent, and A. Kaplan, 2003: Global analyses of SST, sea ice and night marine air temperature since the late nineteenth century. *J. Geophys. Res.*, **108**, 4407, doi:10.1029/2002JD002670.
- Roeckner, E., and Coauthors, 1996: The atmospheric general circulation model ECHAM-4: Model description and simulation of present-day climate. Max-Planck-Institut für Meteorologie Rep. 218, 90 pp.
- Sperber, K. R., 2003: Propagation and the vertical structure of the Madden–Julian oscillation. *Mon. Wea. Rev.*, **131**, 3018–3037.
- Takaya, K., and H. Nakamura, 2001: A formulation of a phase-independent wave-activity flux for stationary and migratory quasigeostrophic eddies on a zonally varying basic flow. *J. Atmos. Sci.*, **58**, 608–627.
- Tam, C.-Y., and T. Li, 2006: The origin and dispersion characteristics of the observed summertime synoptic-scale waves over the western Pacific. *Mon. Wea. Rev.*, **134**, 1630–1646.
- Wang, B., and H. Rui, 1990: Synoptic climatology of transient tropical intraseasonal convection anomalies: 1975–1985. *Meteor. Atmos. Phys.*, **44**, 43–61.
- , and T. Li, 1994: Convective interaction with boundary-layer dynamics in the development of a tropical intraseasonal system. *J. Atmos. Sci.*, **51**, 1386–1400.
- Wang, L., T. Li, and T. Zhou, 2012: Intraseasonal SST variability and air–sea interaction over the Kuroshio Extension region during boreal summer. *J. Climate*, **25**, 1619–1634.
- Wheeler, M. C., and H. H. Hendon, 2004: An all-season real-time multivariate MJO index: Development of an index for monitoring and prediction. *Mon. Wea. Rev.*, **132**, 1917–1932.
- Yang, J., B. Wang, and Q. Bao, 2010: Biweekly and 21–30 day variations of the subtropical summer monsoon rainfall over the lower reach of Yangtze River basin. *J. Climate*, **23**, 1146–1159.
- Zhang, C., 2005: Madden–Julian oscillation. *Rev. Geophys.*, **43**, RG2003, doi:10.1029/2004RG000158.